Aspects of Charge Recombination and Charge Transport in Organic Solar Cells and Light-Emitting Devices

by

Seth Difley

Submitted to the Department of Chemistry
in partial fulfillment of the requirements for the degree of

Doctor of Philosophy

at the

MASSACHUSETTS INSTITUTE OF TECHNOLOGY

February 2010

Author .....
Department of Chemistry
December 18, 2009

Certified by .....
Troy Van Voorhis
Associate Professor of Chemistry
Thesis Supervisor

Accepted by .....
Robert Field
Chairman, Department Committee on Graduate Theses

This doctoral thesis has been examined by a Committee of the Department of Chemistry as follows:

Professor Jianshu Cao .....

Chairman, Thesis Committee

Professor of Chemistry

Professor Troy Van Voorhis .....

Thesis Supervisor

Associate Professor of Chemistry

Professor Andrei Tokmakoff.....

Member, Thesis Committee

Professor of Chemistry

Aspects of Charge Recombination and Charge Transport in Organic Solar Cells and Light-Emitting Devices

by

Seth Difley

Submitted to the Department of Chemistry
on December 18, 2009, in partial fulfillment of the
requirements for the degree of
Doctor of Philosophy

Abstract

In this thesis, aspects of charge recombination and charge transport in organic solar cells and light-emitting devices are presented. These devices show promise relative to traditional inorganic semiconductors. We show that the energy splitting between singlet and triplet CT states in organic materials is appreciable and is material and geometry dependent. This prediction is used to guide the development of an OLED with enhanced fluorescence. The effects of nuclear disorder on optical and transport properties in organic semiconductors are examined and a general computational method for carrying out this analysis is described. The function of organic semiconductors is characterized by the interplay between localized and delocalized excited states. We present an ab initio method for obtaining the electronic coupling between CT states and excitons and discuss the nonadiabatic transitions between these states.

Thesis Supervisor: Troy Van Voorhis
Title: Associate Professor of Chemistry

Acknowledgments

I am grateful to my advisor, Troy Van Voorhis, whose thoughtful guidance has been instrumental in completing this body of work. I also thank Dr. Jianshu Cao and Dr. Andrei Tokmakoff for their service on my thesis committee and for providing advice and inspiration.

I thank:

Jiahao Chen, Xin Chen, Chiao-Lun Cheng, Steve Coy, Jeremy Evans, Ben Kaduk, Tim Kowalczyk, Maksym Kryvohu, Carter Lin, Aiyan Lu, Steve Pressé, Indranil Rudra, Young Shen, XiaoGeng Song, Oleg Vydrov, Lee-Ping Wang, Jianlan Wu, Qin Wu, Sina Yeganeh, Shane Yost, Eric Zimanyi, and other members of the theoretical chemistry graduate student offices (the "Zoo").

Marc Baldo, David Beljonne, Michael Segal, Sergei Tretiak, Lee-Ping Wang, Sina Yeganeh, Shane Yost, and other research collaborators.

Li Mao, Peter Guinta, Anne Hudson, Gloria Pless, Nancy Lyons, and other administrative staff.

Susan Brighton, Melinda Cerny, Mary Turner, and other Chemistry Education Office staff.

Jack Simons, my undergraduate research mentor.

Barbara Grover, Margaret Nielson, Shawna Haider, Hugo Rossi, and other formative instructors.

My friends in the greater New England area and in far flung places for treating me as family.

My parents, brother, and sisters for their love.

Contents

List of Figures

List of Tables

Chapter 1

Introduction

Organic semiconductors (OSCs) are an promising alternative to silicon-based solar cells and LEDs. Organic light emitting devices (OLEDs) convert electricity into light, while organic solar cells, also known as photovoltaics (OPVs) convert light into electricity.[1] Because of the carbon based materials from which these devices are constructed, they can be manufactured using low-cost, high-throughput engineering methods including roll-to-roll and printing processes.[2] OLEDs are useful as high contrast, low power consuming, mechanically tough, versatile, and flexible display materials. Some consumer technologies that make use of OLEDs are computer monitor displays, television screens, cell phones, watch faces, and illuminated computer keyboards. [1]. Meanwhile, OPVs can be used as low weight, highly versatile electrical supplies. With energy conversion efficiencies of 1.7%, OPVs are not expected to replace traditional solar cells in the near future. Instead, proposed uses for these devices include providing electricity for specialized applications such as clothing and packaging where flexibility and durability are priorities. [3, 4, 5]

1.1 Description of organic semiconductors

OLEDs and OPVs are layered devices consisting of donor and acceptor semiconductor layers sandwiched between electrodes. In most of these devices, additional electron and hole transport and blocking layers aid in optimizing the energy conversion effi-

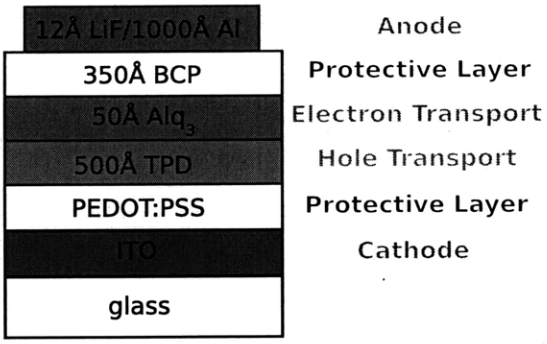

Figure 1-1: Schematic of a multilayer heterojunction OSC. Operating as a photovoltaic, light enters the device at the interface between the electron and hole transport layers and is converted to electrons (e^-) and holes (h^+) that exit at the device leads (anode and cathode). If the device is operating as an OLED, electrons and holes injected the leads are converted into light at the donor-acceptor interface.

ciency (Fig. 1-1). [6] A large variety of OSC materials have been identified. [7]

Each layer serves an important role in In heterojunction solar cell devices, the light must be excite molecules near the EML interface because of the short exciton diffusion lengths in these devices.[8]. The EML is composed of one or more semiconductor materials with band gaps somewhere near the energy of visible light. A large variety of OSC materials have been identified (Fig. 1-2). [7]

Conversion of light to electricity in a typical OPV is a three-step process and is illustrated in Fig. 1-3. In the first step, incident light excites a molecule near the interface between the electron and hole transport layers to generate a localized exciton. Next, the exciton can relax towards a spatially-delocalized CT state, which is a Columbically-trapped electron-hole pair. In the final step, the initially bound electron and hole drift apart and migrate towards the leads where they can collected.

Steps for converting injected charges into light in a heterojunction OLED are similar to the steps for OPV operation, but are in reverse order. Injected charges migrate toward the interface where they form bound CT states. These CT states can undergo charge recombination to form excitons localized onto single molecules. Light is produced when singlet excitons relax to the ground state by fluorescence.

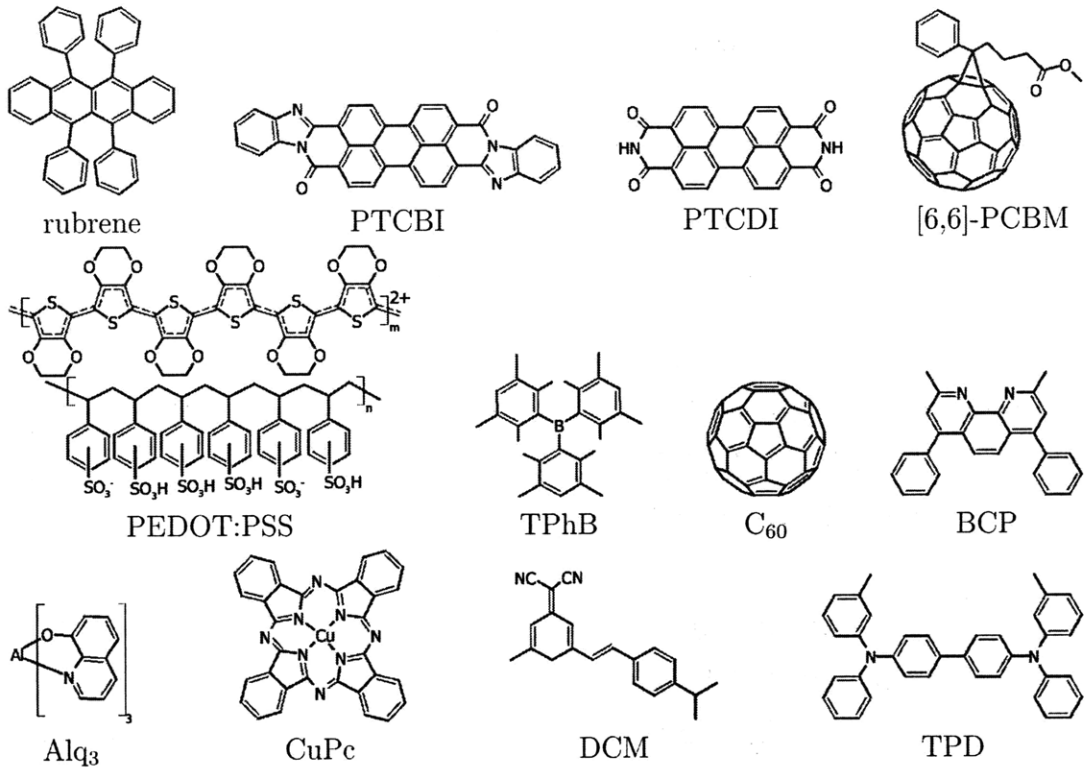

Figure 1-2: Several commonly used organic semiconductor materials.

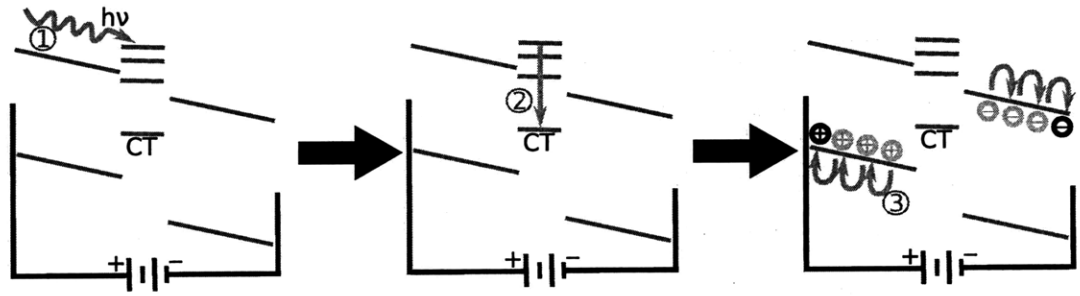

Figure 1-3: 3-step schematic of OPV function. Initial exciton generation by photon absorption (1) is followed by relaxation to form an electron-hole pair CT state (2). After some time, the electron and hole may separate and diffuse by a site-to-site hopping mechanism to the device leads where the charges may be collected (3).

Each layer in heterojunction solar cell devices optimizes one or more of the processes illustrated in Fig. 1-3. Light must excite molecules near the interface because of the relatively short exciton diffusion lengths in these devices. [8]. In addition to choosing materials that promote exciton diffusion, thin device layers are desirable for maximizing the likelihood that an exciton will diffuse to the interface before it

relaxes back to the ground state. In addition, OPV materials near the interface must absorb in the visible light, while OLED materials must emit visible light. A large variety of OSC materials, including small molecules, oligomers, and polymers, have been identified to address these often competing device requirements. [7]

1.1.1 Charge Transport

Charge transport processes are those in which electrons or holes drift from one region to another. [9, 10]. Efficient charge transport is critical to the design of OLEDs and OPVs. In the presence of an applied electric field F, the charge mobility of a carrier with velocity ν is $\mu = \nu/F$. Typical carrier mobilities are in the range $10^{-4} - 10^{2}\frac{cm^2}{Vs}$. Temperature is one of the most important factors influencing carrier mobility. For inorganic semiconductors and in crystalline materials, carrier mobility is found empirically to decrease with increasing temperature. This decreasing carrier mobility is attributed to enhanced phonon scattering processes. In contrast, the presence of disorder in OSCs introduces energy barriers on the order of 0.1-0.5 eV that must be overcome by thermal activation to move charge from one site to another. [11] Thus, OSC carrier mobility tends to increase with temperature.

Disorder and the presence of impurities in OSCs can strongly the carrier mobility by introducing localized trap states. Intramolecular disorder can influence molecular site energies, while disorder in intramolecular positions and orientations leads to variations in the couplings between molecules. The resulting trap states can dramatically influence carrier mobility. For example, variations in the conditions of layer deposition can lead to charge mobilities that span 6 orders of magnitude. [12] Meanwhile, OSC material purification has been shown to produce a four-fold enhancement in pentacene-based device carrier densities. [13]

In addition to temperature, disorder, and impurities, other bulk factors that affect charge mobility include molecular packing, electric field, pressure, molecular size and weight, and charge carrier density. For example, herringbone packing has been shown to increase charge mobility relative to other packing patterns [14]. Meanwhile, hole mobility in P3HT increases by several orders of magnitude as the molecular weight

of the molecule's polymer chain increased. [15]

There are four commonly used experimental methods for obtaining charge mobilities. In the time-of-flight (TOF) method, the material to be studies is placed between two electrodes. Carriers are photoexcited in the material near one of the electrodes and the current at the other electrode is obtained as a function of time. The charge mobilty is given by $\mu = \frac{d^2}{Vt}$, where d is the electrode-electrode distance, V is the applied electric field, and t is the average transient time. For ordered materials, the transient time is sharply peaked and is broadened by structural defects.

A second method for obtaining carrier mobilities is via field-effect transistor configuration. For field-effect transistors (FETs), the current-voltage relationships, respectively, for the linear and saturated regimes are $I_{SD} = \frac{W}{L}\mu C(V_G - V_T)V_{SD}$ and $I_{SD} = \frac{W}{2L}\mu C(V_G - V_T)^2$. Here V_G is the gate voltage, V_T is the threshold voltage for which the current begins to rise, C is the capacitance of the gate dielectric, W and L are the conducting channel's width and length, and I_{SD} and V_{SD} are the current and voltage bias between the source and drain.

Another technique for obtaining carrier mobilities is by diode configuration. In this approach, if carrier trap states are absent, the charge mobility μ is related the current density J, material dielectric constant ϵ_r, and device thickness L by $J = \frac{9}{8}\epsilon_0\epsilon_r\mu\frac{V^2}{L^3}$. The presence of carrier traps in the material leads to a more complex current-voltage relationship and can provide insight about the energetic distribution of trap states within the material.

A fourth experimental approach to obtaining carrier mobilities is pulse-radiolysis time-resolved microwave conductivity (PR-TRMC). Free carriers are generated in the material by a pulse of energetic electrons. The electron pulse changes the electrical conductivity σ of the sample according to $\Delta\sigma = eN_{e-h}\sum\mu$. Here, N_{e-h} is the density of electron-hole pairs produced and is approximately the energy delivered to the system divided by the energy required to produce each electron-hole pair. Mobilities obtained by PR-TRMC are typically upper bounds for low-field mobilities.

In addition to these experimental methods, carrier mobilities can be modeled theoretically. Because intermolecular electronic coupling in OSCs is weak, charge carriers

are localized on single molecules. Therefore, charge transport can be described by a site-to-site hopping mechanism in which carriers hop from one molecule to an adjacent molecule. The efficiency of this process is governed by three parameters: electronic couplings, electron-phonon interactions and site energies. Molecular modeling is important for explaining and predicting how these bulk properties are related to OSC function.

1.1.2 Charge recombination

Charge recombination processes are those in which spatially-separated charges combine to form localized excited states. [16, 17, 18] In fluorescent OLEDs, it is desirable to maximize singlet charge recombination, while charge recombination in organic solar cells is an undesirable energy loss mechanism. The rate of recombination for a given device is dependent on its composition and morphology. Substantial effort has gone into understanding this dependence.[19, 20, 21, 22, 23].

In OSCs, free carriers undergo charge recombination via CT states, which are Coulombically-bound electron-hole pairs. These CT states can be experimentally observed by photoluminescence (PL) measurements if the CT states are coupled to the ground state. In this approach, the CT states are observed as red-shifted bands that are present in the OSC blend, but not in the blend's individual components. [24, 25]. Electroluminescence (EL) also provides evidence of CT states. Here, charge carriers are injected into the device to form the CT state, which can be observed as an emission band present only in the blend. EL studies tend to be more sensitive than PL studies, but both methods require that the CT state be emissive. [26]. For CT states that are weakly emissive, optical absorption methods have been used successfully to identify the CT state. [27]. Evidence suggests that these methods directly excite the ground state to the CT state.[24]. In fact, it was found that the CT state could be directly accessed using sub-bandgap photoexcitation. [28]. Enhanced triplet exciton generation has been given as indirect evidence of CT states. [29] In this argument, singlet CT states undergo intersystem crossing (ISC) to generate triplet CT states which can then undergo charge recombination to form excess triplet excitons.

Charge recombination is characterized as bimolecular or geminate. In geminate recombination, an electron-hole pair is generated from an exciton followed by recombination of the same electron-hole pair to form an exciton. Meanwhile, bimolecular recombination involves the generation of an exciton from an electron and hole that originated on different molecules. Bimolecular recombination typically slower than geminate recombination because it requires that the separated charges diffuse to within the Coulombic capture radius. Geminate recombination occurs on picosecond to nanosecond time scales, while bimolecular recombination may take milliseconds, but can be much faster if high excitation densities are present. [30, 31] As stated previously, bimolecular recombination constitutes a loss mechanism in OPVs. To limit such losses, excitation densities much less than $100\mu J$ are suggested. [16] Charge trapping has also been found to substantially increase recombination. [32, 33]

1.1.3 Density functional theory

Density functional theory (DFT) is an electron structure method that provides ground and excited states that are in excellent agreement with more exact methods, but at a computationally reasonable cost that allows the quantum mechanical simulation of systems containing hundreds of atoms. This balance between computational expense and chemical accuracy has motivated a large body of work on the electronic structure of materials. The basis of DFT is the Hohenberg-Kohn theorem, which states that there is a one-to-one mapping between the external potential $v(\rho)$ and the ground-state wave function Ψ of an electronic system. [34] The ground state energy of a many-electron system with external potential $v(\rho)$ has the electron density $\rho = |\Psi\rangle\langle\Psi|$ that minimizes the functional

$$E[\rho] = \int \rho(r)\, v(r)\, dr + F[\rho], \tag{1.1}$$

where the first term on the right hand side is the electron-nuclear interaction and $F[\rho]$ is the electron-electron interaction. [35] Here, the Born-Oppenheimer approximation is used to separate nuclear and electronic energy contributions. Given

ρ and $v(\rho)$, the electron-nuclear interaction is obtained in straight-forward fashion. Here we summarize how the electron-electron interaction is approximated.

$F[\rho]$ can be partitioned into kinetic and potential contributions $T[\rho]$ and $V_{ee}[\rho]$.

$$F[\rho] = T[\rho] + V_{ee}[\rho]. \tag{1.2}$$

In the Kohn-Sham (KS) DFT treatment, which we use in this work, a noninteracting reference system is introduced that has the same density ρ as the fully interacting system. [36] This allows a further partitioning of the electron-electron interaction into three terms.

$$F[\rho] = T_s[\rho] + J[\rho] + E_{xc}[\rho] \tag{1.3}$$

In Eq. 1.3, $T_s[\rho]$ is the kinetic energy of the noninteracting system and $J[\rho] = \frac{1}{2}\int\int \frac{1}{r_{12}}\rho(\rho_1)\rho(\rho_2)\,dr_1 dr_2$ is the classical electron-electron repulsion energy. $E_{xc}[\rho]$, the exchange-correlation functional, contains the correction between the fully interacting and noninteracting systems.

$$E_{xc}[\rho] = T[\rho] - T_s[\rho] + V_{ee}[\rho] - J[\rho]. \tag{1.4}$$

Eq. 1.3 expresses the exact electronic energy of a fully interacting system with electron density ρ. However, because the exact form of $E_{xc}[\rho]$ is unknown, the exchange-correlation functional is typically approximated. Of the many available approximations, the one that is used in this body of work is the B3LYP hybrid density functional.[37] B3LYP provides ground state properties that are in excellent agreement with experiment for the molecular properties of many systems. However, B3LYP is known to incorrectly describe certain systems, notably charge transfer (CT) states, where long-range charge separation is present. [38]. Many functionals also erroneously predict the transport gap in organic materials. In principle, the energies of the CT states and trasport gap can be tuned by varying the exact Hartree-Fock exchange in the functional. However, choosing the amount of exact exchange that results in correct predictions of excited state energies also results in errors in ground

state energies and equilibrium bond lengths.

1.1.4 Constrained Density Functional Theory (CDFT)

Since TDDFT underestimates CT energies by at least 1 eV for many systems and density functionals [38], we instead use the CDFT approach to obtain CT states. CDFT has been successfully used to study the role of CT states in magnetic exchange and electron transfer. [39, 40, 41, 42, 43]

In the CDFT formalism, we build constraints of the form

$$\sum_{\sigma} \int w_c^{\sigma}(\mathbf{r})\, \rho^{\sigma}(\mathbf{r})\, d\mathbf{r} = N_c \tag{1.5}$$

where the sum is over spins such that $\sigma = \alpha$ or β, c is the constrained region of the system, w_c is a weighting function that corresponds to the constrained property and N_c is the expectation value of the constrained property. Eq. 1.5 is then combined as a Lagrange multiplier constraint with the Kohn-Sham energy functional $E[\rho]$ to generate a new functional

$$W[\rho, \{V_c\}] = E[\rho] + \sum_{c}^{m} V_c \left(\sum_{\sigma} \int w_c^{\sigma}(\mathbf{r})\, \rho^{\sigma}(\mathbf{r})\, d\mathbf{r} - N_c \right), \tag{1.6}$$

where the c^{th} Lagrange multiplier is V_c, and there are m constraints. W is then made stationary with respect to ρ and V_c. By this procedure, we obtain the energy $E(\rho)$ as a natural function of the expectation value N_c.

1.2 Thesis Overview

In Chapter 2, we use DFT to examine properties of the singlet-triplet CT energy splitting in OSC materials and discuss the implications of these results on OLED design. Chapter 3 presents experimental results that show how Chapter 2's results can be used to design OLED devices with enhanced fluoresence efficiency. Chapter 4 presents a QM/MM method for tackling the problem of nuclear disorder in OSC ma-

terials and presents results for the archetypal OLED material Alq_3. The interactions between CT states and exciton play crucial roles in the function of OSCs. Chapter 5 presents a method for obtaining the electronic coupling between these spatially-localized and delocalized states. In Chapter 6, we discuss future directions for this research.

Chapter 2

On the singlet-triplet splitting of geminate electron-hole pairs in organic semiconductors

2.1 Introduction

Due to their unusual mechanical and photophysical properties, organic semiconductors show promise in the development of a variety of innovative technologies: inexpensive light emitting devices [44], flexible transistors [45] and novel photovoltaic architectures[46], just to name a few. Typically, these organic materials involve weakly bound assemblies of π-conjugated molecules or polymers whose electro-optical properties rest on a complex interplay between electron transfer kinetics[9], organic photochemistry [47] and organic/inorganic interfacial structure [48]. In the search for improved performance, chemistry plays a central role by providing information about the participating states - including their formation rates, lifetimes, and decay pathways - ultimately facilitating the rational design of novel devices.

Of special interest in this context are the charge transfer (CT) states that determine both the transport properties of the material and the exciton dissociation and recombination rates that govern electroluminescent and photovoltaic efficiency [49].

In particular, CT excited states play a crucial role is in the operation of organic light emitting devices (OLEDs) [50, 51, 52, 53]. OLED-based display technologies are a promising alternative to traditional inorganic LED-based displays because they can be brighter, more adaptable, longer-lived, and more energy efficient. Basic OLEDs consist of a solid-state emitting layer (EML) containing electron- and hole-accepting molecules sandwiched between an anode and a cathode [54]. Electrons (holes) injected at the cathode (anode) enter the EML and diffuse through it, eventually migrating onto adjacent molecules to form a CT state, which is an intermolecular charge-separated donor-acceptor pair (D^+A^-). Once the CT state has formed, it is bound by the Coulombic force that results from the charge separation. Because the electron and hole are both spin-1/2, the CT state will be either a singlet or triplet. Sometime after CT state formation, the electron and hole may undergo charge recombination to form an exciton that will typically have the same spin symmetry as the CT state. Singlet excitons can undergo efficient fluorescent decay to the ground state, while triplet excitons decay to the singlet ground state by phosphorescence, an inefficient process in the absence of spin-orbit coupling [55]. Thus, the question of spin statistitics - what fraction of excitons are created as singlets as compared to triplets - plays a key role in OLED efficiency.

Assuming that the CT states are formed from electrons and holes having a random distribution of spin symmetry, three triplet CT states will be formed for each singlet CT state. If intersystem crossing (ISC), which interchanges singlet and triplet CT states, is negligible, the fraction of singlet excitons formed will be 1/4 and the expected fluorescent efficiency will be 25%. The literature does contain numerous reports where this simple statistical limit is actually observed [56, 57], but there are also multiple reports of >25% fluorescent efficiency [58, 59, 60, 61, 62, 63, 64] and a variety of theoretical work has been conducted on OLED exciton formation [65, 66, 67, 68, 69, 70, 71, 72, 73, 74, 75] to address these observations.

The conventional picture of enhanced fluorescence that emerges from this work, first postulated in Ref.[65], (see Figure 2-1) focuses on the rate of triplet exciton formation, k_T. One notes that the driving force for triplet charge recombination,

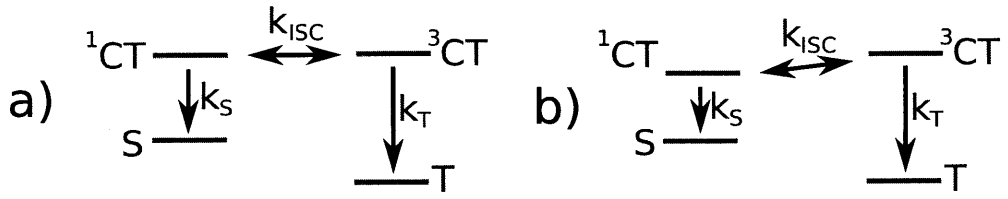

Figure 2-1: Exciton formation pathways assuming nearly degenerate CT states (a) and $\Delta E_{ST} < 0$ (b). Singlet and triplet excitons are, respectively, labeled S and T.

$\Delta G_T \equiv E_{CT_T} - E_T$, for an organic dye or oligomer is typically .5-.7 eV greater than its singlet counterpart, $\Delta G_S \equiv E_{CT_S} - E_S$ [76, 77]. Further, electron transfer for these materials typically occurs in the Marcus inverted region because the energy gaps involved are many times the associated reorganization energies. Thus, the recombination rate is expected to *decrease* as the energy gap *increases*. From these observations, the conventional view predicts that triplet exciton formation will be much slower than the analogous singlet rate, $k_T \ll k_S$, because $\Delta G_T \gg \Delta G_S$. As a result, one could potentially obtain efficiencies that exceed 25% if the ISC rate, k_{ISC}, is competitive with the rate of triplet exciton formation, k_T but much less than the corresponding singlet rate, k_S. That is, fluorescence is enhanced if $k_S \gg k_{ISC} \geq k_T$. On the other hand, if k_T is faster than k_{ISC} (though it may still be slower than k_S) an efficiency of 25% could be observed. One problematic point of this interpretation is that it leads one to assume that high efficiency fluorescence should occur when ΔG_T is large, and that statistically expected 25% efficiency will occur for small ΔG_T. However, this correlation has not been observed in practice. To explain this, it has been proposed that in cases where the statistical limit is observed, dark triplet states between the triplet exciton and ground state can make k_T much faster than it otherwise would be [49], thereby exceeding the intersystem crossing rate and leading to the formation of a 1:3 ratio of singlet to triplet excitons.

In this paper, we examine an alternative hypothesis for the variation of singlet formation efficiencies, which focuses on the variation of k_{ISC} between different organic semiconducting materials. In particular, while there are many processes which will influence this rate in real systems (e.g. spin-orbit coupling, spin-lattice relaxation, hyperfine interactions...) which are quite difficult to compute, there is one

factor which can be simulated - the singlet-triplet CT energy gap (ΔE_{ST}). In particular one expects that, as suggested previously [78], if ΔE_{ST} is sufficiently large k_{ISC} (Figure 2-1 bottom) will be very slow relative to both k_S and k_T and the resulting singlet-triplet exciton formation ratio will be 1:3. Meanwhile for small ΔE_{ST}, the fluorescence efficiency could still exceed 25% in the standard way (Figure 2-1 top). Thus, in this view, the material and geometry dependence of ΔE_{ST} can play a crucial role in determining the fluorescence efficiency of a given device. To examine the validity of this picture, we use simulations to estimate the singlet-triplet CT state splitting, ΔE_{ST}, in dimers of several low to medium weight chromophores and oligomers and discover several surprising results. First, ΔE_{ST} is strongly material dependent, changing magnitude and even sign depending on the system being studied. Second, in contrast with the commonly held view, we find that the singlet CT state nearly always lies below the triplet CT state ($\Delta E_{ST} < 0$). This result is explained in terms of two related physical properties. First, at the short intermolecular distances present in CT states, the exchange interaction is dominated by kinetic exchange, which favors the singlet state. Second, Coulombic interaction within the CT state causes reorganization that decreases the distance between the electron and hole and further increases the singlet-favoring kinetic exchange. Implications of these results on the design of efficient OLEDs are discussed. In particular, our finding that ΔE_{ST} is generally nonzero suggests that OLEDs typically will experience slow intersystem crossing and, therefore, low fluorescence efficiency if spin orbit coupling is absent. However, as recently shown [79], the insertion of a sensitizer that mixes the CT states while leaving the exciton states unmixed leads to a much more efficient OLED.

2.2 Methods

2.2.1 Constrained density functional theory

We use constrained density functional theory (C-DFT) to compute the singlet-triplet gaps in CT states. The details of this approach, which uses constraints to com-

pute both charge transfer excited states and exchange couplings, have been detailed elsewhere [39, 40]. Here, we briefly review C-DFT and illustrate the use of this computational tool.

In the C-DFT formalism, we build constraints of the form

$$\sum_{\sigma} \int w_c^{\sigma}(\mathbf{r})\, \rho^{\sigma}(\mathbf{r})\, d\mathbf{r} = N_c \tag{2.1}$$

where the sum is over spins such that $\sigma = \uparrow$ or $\downarrow$, c is the constrained region of the system, w_c is a weighting function that corresponds to the constrained property and N_c is the expectation value of the constrained property. Eq. (2.1) is then combined as a Lagrange multiplier constraint with the Kohn-Sham (KS) energy functional $E[\rho]$ to generate a new functional

$$W[\rho, \{V_c\}] = E[\rho] + \sum_{c}^{m} V_c \left(\sum_{\sigma} \int w_c^{\sigma}(\mathbf{r})\, \rho^{\sigma}(\mathbf{r})\, d\mathbf{r} - N_c \right), \tag{2.2}$$

where the c^{th} Lagrange multiplier is V_c, and there are m constraints. W is then made stationary with respect to ρ and V_c. By this procedure, we obtain the energy $E(\rho)$ as a natural function of the expectation value N_c. The utility of this method has been previously demonstrated for studying magnetic exchange couplings using spin constraints [40] and to obtain Marcus parameters [42, 43] and study long range electron transfer [41] using charge constraints.

In the present study of CT state singlet-triplet splittings, both charge and spin constraints are used. These calculations are performed on a supersystem containing a donor and an acceptor molecule. Two separate constrained calculations are performed on the donor-acceptor system, one in which the excess spins are parallel ($\uparrow\uparrow$) and one in which they are anti-parallel ($\uparrow\downarrow$). Note that the $\uparrow\downarrow$ configuration will be referred to as the "mixed" state because it is a mixture of $M_S = 0$ singlet and $M_S = 0$ triplet spin states. The $\uparrow\uparrow$ configuration will be referred to as the triplet state. A charge constraint is applied that forces the acceptor to have an excess charge of -1. A concurrent constraint on the net spin forces the donor and acceptor, respectively, to have excess spin of $\pm\frac{1}{2}$. Since the spin component of the singlet state is $\frac{1}{\sqrt{2}}(|\uparrow\downarrow\rangle - |\downarrow\uparrow\rangle)$, the

singlet-triplet gap ΔE_{ST} is twice the energy difference between the parallel and anti-parallel states [80].

$$\Delta E_{ST} = 2\left(E_{\uparrow\downarrow} - E_{\uparrow\uparrow}\right) \tag{2.3}$$

These calculations neglect the effects of neighboring molecules on the active dimer. That is, crystal packing constraints and outer sphere reorganization are absent from our model. However, our models do consider the contribution of the inner sphere reorganization to the CT state splitting in these systems.

2.2.2 Computational Details

Constrained calculations were performed using versions of NWChem[81] and QChem[82] in which C-DFT has been implemented. All calculations described herein were computed using the B3LYP hybrid functional. Meanwhile, the LANL2DZ effective core potential (ECP) was employed when necessary. The 3-21G basis set was used unless otherwise indicated. When dimer crystal structures were available, these were taken to be the neutral state geometries. In cases where crystal structure geometries were unavailable, a geometry guess was constructed by placing the donor and acceptor at a reasonable long-range distance of about 3.5 Å and oriented such that the ground state HOMO orbital on the acceptor was in the proximity of the ground state LUMO on the donor. CT state geometries were obtained by optimizing this initial geometry subject to the corresponding population constraints. The geometries used in these calculations are available in the supporting materials. The weighting function $w_c(\mathbf{r})$ in Eq. (2.2), which measures the net charge and spin, may be reasonably defined in several ways. The calculations presented here use the definition of Becke [83].

In this article, we study the CT system in the moment immediately before charge recombination and the geometry of the system in this configuration can have a significant influence on the energetics. When the system is promoted from neutral to CT, relaxation toward the CT state's optimal geometry will naturally occur. If the charge

transfer process is fast relative to this reorganization, the relevant charge recombination geometry will be near the initial, neutral state geometry. On the other hand, if the charge transfer process is slow relative to reorganization, the relevant geometry is expected to be nearer to the CT state optimal geometry. Since the relative rates of these processes are not known, it is useful to compute splittings in both limits.

2.3 Results

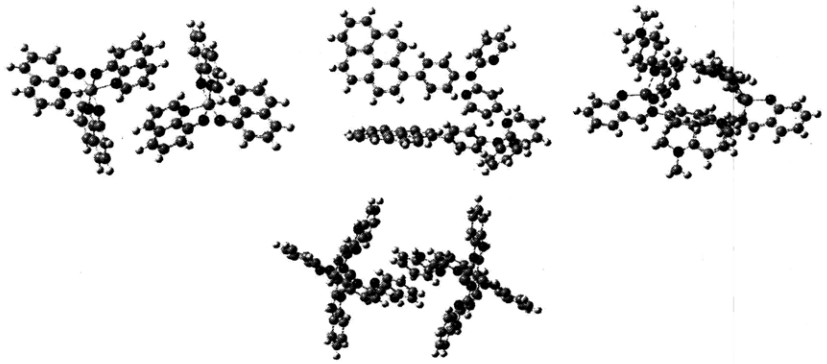

Figure 2-2: Representative dimer structures from Table 2.2. From left to right, α-Alq_3, 4-(1-pyrenyl)phenyl-2,2′-dipyridylamine, $Zn(sada)_2$ and $[Zn(tpy)_2]^{2+}$.

To grossly characterize the behavior of ΔE_{ST} for organic chromophores, we computed the splitting for a series of homonuclear dimers formed from low-molecular weight dyes. For reference, representative structures of these dimers are shown in Figure 2-2. Alq_3 was chosen because it is the prototypical material used as the emitting layer in many model OLEDs [79]. Here, there are three different polymorphs of the crystal with slightly different photophysical properties. In particular, the δ phase consists of the *fac* isomer of Alq_3 - as opposed to the *mer* isomer present in the α and β phases. The change in monomer structure and reduced π interaction in the excited state gives rise to a blueshift in the spectrum, making δAlq_3 a blue emitter [84, 85]. The dipyridylamine (dpa) complexes were chosen because of their unusual ability to emit in the deep blue [86]. $Zn(sada)_2$ thin films show more common yellow emission with improved charge transport characteristics[87]. The final three zinc complexes demonstrate the interesting behavior that the crystal packing has a

significant influence on the monomer geometry (i.e. the molecule is more flexible) which could lead to interesting effects[88]. Thus, these crystals allow us to test the degree to which different bonding motifs and photophysical properties influence or at least correlate with ΔE_{ST}.

For reference, calculated and experimental singlet and triplet exciton energies for these materials are presented in Table 2.1. The TDDFT calculations are vertical excitation energies obtained for isolated monomers taken from the crystal structure. As a result, the theoretical predictions neglect a number of features (e.g. crystal field effects, exciton delocalization, etc.) that are known to be necessary for the accurate prediction of solid state excitation spectra. Further, we note that not all the experimental numbers are precisely comparable to one another; in some cases the experiments were done in crystals, others in thin films and still others in solution. Taking all these points into consideration, one should really consider the calculated numbers and experiments as ballpark estimates of the energies involved here. In this context, TDDFT does a fairly good job of predicting the exciton energies in these materials, typically predicting the exciton energies to within .2-.3 eV.

	TDDFT (eV)		Δ_{SCF}(eV)	Expt. (eV)	
Chromophore	S	T	T	S	T
α-Alq_3	2.7 (2.7)	2.2 (2.2)	2.4 (2.4)	2.9[1]	2.1[2]
δ-Alq_3	2.8 (2.9)	2.2 (2.2)	2.3 (2.3)	2.9[3]	2.2[2]
1-R_1-dpa	3.5 (3.4)	2.5 (2.4)	2.5 (2.5)	3.6[4]	–
4-R_2-dpa	3.4 (3.4)	2.4 (2.3)	2.5 (2.4)	3.6[4]	–
4-R_3-dpa	3.0 (3.0)	2.4 (2.4)	2.5 (2.4)	3.6[4]	–
$Zn(sada)_2$	2.9 (2.9)	2.3(2.3)	2.4 (2.4)	2.6[5]	–
$[Zn(bbp)_2]^{2+}$	3.5 (3.3)	2.9 (2.8)	3.1 (3.0)	–	–
$[Zn(tpt)_2]^{2+}$	2.4 (2.7)	2.2 (2.6)	2.9 (3.1)	–	–
$[Zn(tpy)_2]^{2+}$	3.4 (4.1)	3.2 (3.3)	3.7 (3.4)	–	–

[1] absorption onset in crystal[89]
[2] phosphorescence in crystal[90]
[3] absorption onset in crystal[84, 85]
[4] absorption maximum in THF[86]
[5] absorption onset in thin film[87]

Table 2.1: Calculated and experimental singlet (S) and triplet (T) exciton energies for the chromophores in Table 2.2. TDDFT calculations were perfromed with B3LYP in the 3-21G basis. 6-31G* results are shown in parenthesis.

Next, we turn our attention to the intermolecular CT excited states of these materials. Here we employ constrained DFT, as described in the previous section. Each calculation was performed on a dimer formed from near-neighbor monomers oriented according to the crystal structure. Splittings were obtained for both the 3-21G and 6-31G* basis sets and the results are compiled in Table 2.2. Noting that a negative ΔE_{ST} means that the singlet CT state lies below the triplet CT state, we observe that singlet CT states are stabilized relative to triplet CT states for all of these systems in their crystal structure geometries. This observation contrasts with the general assumption that triplet CT states lie lowest [76, 77, 91]. Further, we find that splittings predicted in the two basis sets are similar in both sign and magnitude. While this could potentially be due to a cancellation of errors between the two basis sets, the consistency of the agreement strongly suggests instead that Δ_{ST} is insensitive to basis set, so that our results can be considered nearly converged with respect to basis set size. Importantly, the resulting magnitude of ΔE_{ST} implies that intersystem crossing (Figure 2-1) should be much slower than one would expect from nearly-degenerate spin pairs.

While the sign of the splitting is constant across the cases, we find that the magnitude can change significantly from system to system. Further, based on these data alone it is very difficult to provide case-by-case explanations for why some materials have large splittings and others do not. The variations of ΔE_{ST} *within* a given structural motif are at least as large as the variations *between* different motifs. For example, comparing the three Alq_3 phases in Table 2.2, we observe that modification of the orientation of the monomers can result in differences in the singlet-triplet CT gap by more than an order of magnitude. Perhaps surprisingly, the exchange splitting does not correlate with the inter-monomer distance, as evidenced by examining the metal-metal distances shown in Table 2.2. Rather, it appears that the relative orientation of donor and acceptor plays a more significant role. All of these observations lead to the conclusion that ΔE_{ST} shows strong non-trivial material dependence. The one exception to this may be $Zn(sada)_2$. This material has the largest splitting of any of the compounds and also has the best transport properties. Based on the kinetic

Chromophore	ΔE_{ST} (meV) 3-21G	6-31G*	Metal-Metal Distance (Å)	$\mu_{\uparrow\downarrow} - \mu_{\uparrow\uparrow}$ (Debye)
α-Alq_3 [a]	-2	-2	8.86	0.07
β-Alq_3 [a]	-6	-7	11.28	0.00
δ-Alq_3 [b]	-60	-74	8.87	0.11
1-R_1-dpa [c]	-58	-61	–	0.02
4-R_2-dpa [c]	-1	-5	–	0.00
4-R_3-dpa [c]	-30	-42	–	0.00
$Zn(sada)_2$ [d]	-102	-102	8.97	-0.10
$[Zn(bbp)_2]^{2+}$ [e]	-67	-57	8.67	0.04
$[Zn(tpt)_2]^{2+}$ [e]	-19	-48	8.95	-0.03
$[Zn(tpy)_2]^{2+}$ [e]	-85	-89	8.79	-0.23

[a] Alq_3 = tris(8-hydroxyquinoline)aluminum(III)[89]
[b] Alq_3 = tris(8-hydroxyquinoline)aluminum(III)[84]
[c] dpa = 2,2′-dipyridylamine, R_1 = pyrenyl, R_2 = (1-pyrenyl)phenyl, R_3 = 4′-(1-pyrenyl)biphenyl [86]
[d] $Zn(sada)_2$ = bis[salicylidene(4-dimethylamino)aniline]zinc(II) [87]
[e] bbp = 2,6-bis(1*H*-benzimidazol-2-yl)pyridine, tpt = 2,4,6-tris(2-pyridyl)-1,3,5-triazine, tpy = 2,20′:6′,2″-terpyridine [88]

Table 2.2: ΔE_{ST} for dimers of several low-molecular weight chromophores computed using 3-21G and 6-31G* basis sets. Metal-metal bond distances and differences between $\uparrow\downarrow$ and triplet dipole magnitudes are also presented.

exchange mechanism we propose below, we expect this is not a coincidence - materials with high mobilites may tend to have large ΔE_{ST} as well, as both properties tend to result from good donor-acceptor overlap. Finally, we note the interesting fact that α- and β-Alq_3 have nearly degenerate CT states, implying that intersystem crossing could be favorable for these systems (see Figure 2-1), while for the δ-Alq_3 phase, intersystem crossing should be quite strongly hindered.

Overall, the inclusion of the variation of other components of k_{ISC} (e.g. spin-orbit or hyperfine coupling constants) would typically increase the material dependence of these rates. Thus, one expects that the conclusion of strong material dependence of k_{ISC} will not change qualitatively if more sophisticated treatments of spin relaxation are employed.

To explain how singlet CT states can lie below triplet CT states, we invoke the physical picture of kinetic exchange. Kinetic exchange is a two-step mechanism that

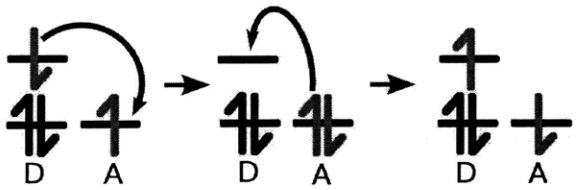

Figure 2-3: Kinetic exchange mechanism showing electron exchange between the donor (D) monomer's LUMO and acceptor (A) monomer's HOMO.

swaps the unpaired electrons in the CT state (Figure 2-3) and has a spin-paired intermediate state. In contrast, direct exchange swaps the electrons in a single step without pairing them. Using perturbation theory and ignoring weaker contributions such as superexchange, it has been shown [92] that the singlet-triplet splitting should be given by

$$\Delta E_{ST} = -\frac{t^2}{\Delta E} + K, \tag{2.4}$$

where the first and second terms are, respectively, due to kinetic and direct exchange. Here, t is a hopping term between the donor and acceptor, ΔE is an energy difference between the initial and virtual states in the system, and K is a positive exchange integral. The negative sign of the kinetic exchange term corresponds to stabilization of the singlet state relative to the triplet. This stabilization can be thought of as a result of the singlet unpaired electrons lowering their energy by occasionally visiting the same region of space to form the paired intermediate shown in Figure 2-3. Meanwhile, the triplet unpaired electrons cannot visit the same region of space due to the Pauli exclusion principle and therefore cannot undergo a similar stabilization.

To make use of Eq. 2.4, we approximate the hopping term, t, by the overlap, S, between an orbital on the donor and an orbital on the acceptor and assume that ΔE and K do not vary strongly with geometry. Then the variations in ΔE_{ST} will be approximately proportional to S^2 for systems that are dominated by kinetic exchange. Discrepancies from proportionality may be attributed to contributions from other exchange mechanisms [93, 92, 94] such as direct, indirect, and superexchange or to a non-constant value of ΔE. Using this expectation of proportionality, kinetic exchange contributions were examined for homonuclear CT state dimers of two molecules, poly-

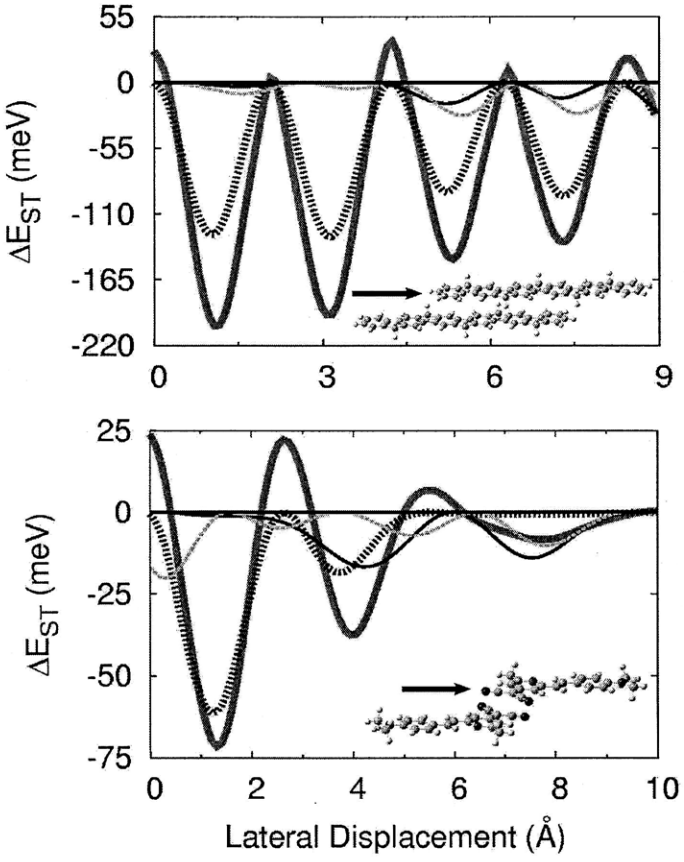

Figure 2-4: ΔE_{ST} (thick solid red curve) and squared orbital overlaps for poly-*p*-phenylene (top) and DCM (bottom) as a function of lateral monomer displacement. Squared overlaps shown in arbitrary units: HOMO/LUMO (thick dashed blue), HOMO-1/LUMO (thin solid black), and HOMO/LUMO+1 (thin dashed green).

p-phenylene oligomer [95], intended to mimic a high molecular weight polymer, and DCM (4-dicyanomethylene-2-methyl-6-*p*-dimethylaminostyryl-4H-pyran) [96], a low molecular weight dye. Dimers of each molecule were generated by combining ground state geometry-optimized monomers in head-to-tail orientation. The planar distances between monomers in the DCM and phenylene dimers, respectively, were 3.50 and 3.65 Å, which represent reasonable monomer separations for near-neighbor CT states. The monomers of each dimer were given initial relative orientations and incrementally displaced laterally relative to each other. For each step of this lateral displacement, splittings and donor-acceptor orbital overlaps were computed. (Figure 2-4). These orbital overlaps were obtained by performing single point ground state calculations on each monomer separately to yield molecular orbitals ϕ_D and ϕ_A, respectively, for the isolated donor and acceptor monomers. These unrelaxed orbitals were then rigidly shifted relative to one another to obtain the overlaps at various relative displacements.

For both DCM and poly-*p*-phenylene, Figure 2-4 shows that ΔE_{ST} and the HOMO/LUMO squared overlap are nearly proportional, indicating that kinetic exchange is the dominant exchange mechanism in these CT state systems. Meanwhile, there is no obvious relationship between ΔE_{ST} and the other orbital overlaps examined in Figure 2-4, suggesting that interaction between the HOMO and LUMO has a key role in kinetic exchange. Finally, since kinetic exchange only stabilizes the singlet CT state, the observed dominance of this exchange mechanism serves as an explanation of why the CT state splittings have been found to be almost always negative and suggests that these results are not simulation artifacts.

Let us now consider the effects of allowing the CT state to undergo geometry relaxation. While crystal packing will generally reduce these effects by preventing full relaxation, the direction of the shift should be important. That is, if it is found that geometry relaxation stabilizes singlet CT states more than triplet CT states, it will support the previous conclusion that singlet CT states most often lie below triplet CT states. On the other hand, if geometry relaxation is found to destabilize the singlet CT state relative to the triplet CT state, it will suggest that, even if splittings obtained in the crystal structure geometry favor singlet CT states as in

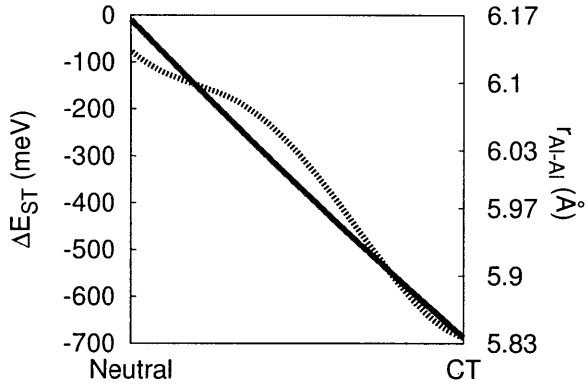

Figure 2-5: ΔE_{ST} (dotted line) and Al-Al distance (solid line) as a function of linear reaction coordinate connecting the crystal structure geometry (Neutral) with the optimized $\uparrow\downarrow$ CT state geometry (CT) for the α-Alq_3 dimer. We see that as geometry relaxation proceeds, the magnitude of ΔE_{ST} increases while the Al-Al distance decreases.

Table 2.2, the singlet CT state in the actual system may or may not be favored once partial relaxation has occurred.

To examine these issues, the optimal CT geometry was computed for Alq_3 beginning from the crystal structure for α-Alq_3 and relaxing the dimer in the mixed ($\uparrow\downarrow$) CT state. The mixed state was chosen because it presents an idea of the "average" structures assumed by the singlet and triplet CT states. An approximate reaction coordinate was constructed by linear interpolation between the crystal structure geometry and the $\uparrow\downarrow$ CT state geometry and ΔE_{ST} was computed as a function of this reaction coordinate, as shown in Figure 2-5. We observe that the singlet CT state lies below the triplet CT state along the entire coordinate and that the splitting increases monotonically as we proceed from the crystal structure to the CT structure. We can rationalize this singlet stabilization by noting that the Coulombic attraction present in the CT state causes the donor-acceptor distance to decrease as relaxation occurs (See Figure 2-5). This decreased distance results in increased orbital overlap, which causes an increase in kinetic exchange and thereby increases the singlet stabilization. We note that direct exchange should also increase in magnitude as the monomers approach one another, although apparently more slowly than the kinetic term. Additional evidence of this singlet stabilization trend was obtained by computing mixed

Dimer	$\Delta E_{ST}(q_{\uparrow\downarrow})(meV)$
FIrpic$^-$:DCM2$^+$ [a]	-116
DCM$^-$:CBP$^+$ [b]	-329
α-Alq$_3^-$:PtOEP$^+$ [c]	-323

[a] Firpic = iridium(III)bis [(4,6-di-fluoropheny)-pyridinato-N,C$^{2\prime}$]picolinate [98], DCM2 = 4-dicyanomethylene-2-methyl-6-[2-(2,3,6,7-tetrahydro-1H,5H-benzo[ij]quinolizin-8-yl)vinyl]-4H-pyran[99]
[b]CBP = 4,4′-bis(9-carbazolyl)-2,2′-biphenyl [100]
[c]PtOEP = 2,3,7,8,12,13,17,18-octaethyl-21H,23H-porphine platinum (II) [101]

Table 2.3: Adiabatic ΔE_{ST} for several CT state heterodimers at the relaced $\uparrow\downarrow$ CT geometry. Structura relaxation causes substantial stabilization of singlets over triplets.

CT state optimized geometry splittings for three heterodimers (Table 2.3) selected because of their chemical relevance to the design of extrafluorescent OLEDs [79]. For each of these dimers, we again find that the splitting at the CT geometry strongly favors the singlet. We note that, while DFT tends to give unreliable structures for van der Waals complexes in general [97], the relaxed CT geometries are dominated by charge-charge interactions between donor and acceptor and as such should be well approximated by DFT. These results imply that, for systems in which singlet CT states are favored in the ground state geometry, the singlet CT will be even more strongly favored as relaxation toward the CT state geometry occurs.

2.4 Discussion

Two experimental measurements of ΔE_{ST} for geminate electron-hole pairs in organic materials exist in the literature. Segal *et al.* [79] electrically excite an OLED containing Alq$_3$ and PtOEP to obtain $\Delta E_{ST} = -7$ meV. That is, they find the singlet CT state for that device to lie below the triplet CT state, in agreement with the energy ordering of the crystal structure and geometry optimized splittings presented in Tables 2.2 and 2.3. On the other hand, Kadashchuk *et al.* [102] photoexcite poly-*p*-phenylene and measure its electroluminescence efficiencies as a function of temperature to find that the triplet CT state lies 3-6 meV below the singlet CT state, which has the opposite energy ordering of the majority of our calculations. However, since the mag-

nitude and sign of the splitting has been found to be geometry dependent (Figure 2-4), it is not unreasonable to suggest that the donor-acceptor structure studied by Kadashchuk may be the exceptional case where triplets are favored.

In either case, it is observed that the calculated splittings are typically an order of magnitude larger than the experimental splittings. Obviously, one concern is that this discrepancy arsies from a systematic theoretical error. Most importantly, one notes that the CT states are diradicals, which are typically treated poorly in DFT because of nondynamic correlation[103]. While we cannot completely rule out these effects in the present case without significant computational expense (e.g. CASTPT2), we do note that constrained DFT is expected to reduce the influence of nondynamic correlation on the results [40]. In fact, simulations of the type presented here have been shown to have typical errors of only 10-20 meV for transition metal exchange couplings [40], so that the discrepancy in magnitude between theory and experiment is not expected to be due to the simulation method. Instead, it can be understood by recognizing that in a real device next-nearest and next-next-nearest neighbor CT states are generated along with their near-neighbor counterparts whereas the splittings calculated here correspond only to nearest neighbor donor-acceptor pairs. To put it another way, the experiments probe an *ensemble* of structures of which we have considered only one representative. Since the magnitude of the splitting generally decreases with donor-acceptor pair orbital overlap and overlap decreases with pair distance, the splittings calculated here are expected to provide upper bounds for experimentally measured splittings. Thus, our results indirectly suggest that next-nearest and next-next-nearest neighbor CT states may play a significant role in these devices, a point than has not previously been appreciated. However, since we do not see a strong dependence of the *sign* of the splitting on distance (Table 2.2), our qualitative conclusions should remain valid even for non-nearest neighbors.

The effects of the surrounding environment on CT state splittings have so far not been addressed, where the interactions to consider include steric, electrostatic, and van der Waals forces. In principle, the effects of steric interaction on the splitting could be studied by computing geometry optimized splittings for systems containing

nearest neighbor and next nearest neighbor monomers. However, calculations on such large systems are generally computationally impractical, and as noted earlier, their effect would primarily be to reduce reorganization. However, since CT states contain a spatially separated electron and hole, they are expected to have large dipoles and to couple with polarizable groups in their vicinity. In other words, CT states are expected to have strong electrostatic interactions with their surroundings. We studied the effects of these interactions on the splitting in two ways. First, the dipoles of the singlet and triplet CT states were compared for each of the dimers in Table 2.2 where the difference in magnitudes between the singlet and triplet dipole moments is also shown. When this difference is small, the singlet and triplet state energies are expected to undergo similar relaxation in the presence of electrostatic interactions, thereby leaving ΔE_{ST} unaltered relative to the splitting obtained in vacuum. Note that the largest difference in dipole magnitude occurs for the $[Zn(tpy)_2]^{2+}$ homodimer, suggesting that it may be the most susceptible of these dimers to electrostatic interactions. To study this susceptibility more rigorously, the COSMO dielectric continuum model [104] with a dielectric constant of $\epsilon = 3$ was used to approximate the electrostatic effect on the donor-acceptor pair due to surrounding monomers. For the $[Zn(tpy)_2]^{2+}$ homodimer, the splitting with (without) the dielectric continuum was -73 meV (-85 meV). The similarity between the splittings obtained with and without a dielectric suggest that electrostatic interactions should not materially affect our conclusions even with modest differences between the singlet and triplet dipole magnitudes. This result is reasonable because ΔE_{ST} is a comparison of one CT state to another rather than a comparison of a CT state to the ground state, where dielectric effects would be expected to be larger. The final class of forces one might consider is van der Waals interactions. These forces are expected to be much weaker than either sterics or electrostatics and thus their effect on the splitting is not studied in detail here.

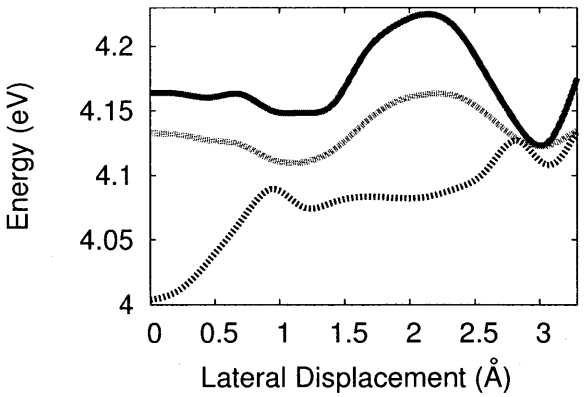

Figure 2-6: Excited state of poly-*p*-phenylene as a function of lateral displacement using INDO/SCI. In order of increasing energy, the states shown are second singlet exciton (dashed blue), triplet CT state (dotted magenta), and singlet CT state (solid red).

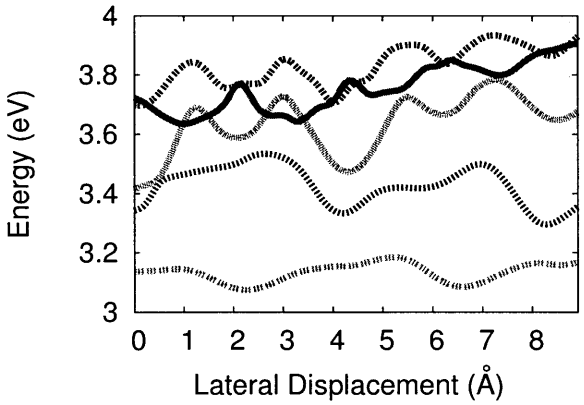

Figure 2-7: Excited state of poly-*p*-phenylene as a function of lateral displacement using TDDFT. In order of increasing energy, the states shown are the first singlet exciton (dot-dashed orange), second singlet exciton (dashed blue), third singlet exciton (dotted magenta), singlet CT state (solid red) and triplet CT state (dashed black).

The simulations described so far allow mixing between the CT states, but do not consider the possibility that mixing might also occur between CT and high-lying exciton states. To put it another way, the constrained calculations assume that a full unit of charge has transfered from the donor the acceptor, whereas one should expect a certain amount of leakage of the excess charge back on to the donor. Such mixing

or leakage could increase charge recombination rates or induce intersystem crossing. To study this possibility, poly-*p*-phenylene was laterally displaced as in Figure 2-4 and energies for the CT and singlet exciton states were obtained using INDO/SCI [105, 106] (Figure 2-6) and TDDFT [107] (Figure 2-7). We note that TDDFT by itself does not accurately predict the CT excitations in this system, placing them more than 1 eV too low [103]. Hence only the *intramolecular* excited states are described here with TDDFT, while the CT states are obtained from CDFT, as before. Figure 2-6 shows avoided crossings of the CT and second exciton states at ≈1 and ≈3 Å using INDO/SCI. Thus, significant mixing is expected at these geometries. Meanwhile, if we compare the TDDFT exciton energies with the C-DFT CT state energies, we see that the curves cross at ≈1 and ≈3 (also ≈5 and ≈7) Å. As noted previously [41], the DFT curves do not avoid one another because C-DFT states correspond to diabatic states which can undergo surface crossing. These four lateral displacements correspond to the four minima of ΔE_{ST} in the top figure of Figure 2-4. These results suggest that when the singlet CT state is most stabilized, non-luminescent exciton states can come quite close to the CT state and may play a significant role in the recombination process. We plan to investigate this process more fully in a later paper. For the present, we merely note that our results so far support the hypothesis that ΔE_{ST} plays a significant role in the recombination process but they do not disprove the possible further interference of dark excitons in the dynamics [49].

Fluorescence efficiency within OLEDs is directly related to the fraction of singlet exciton states produced because only those states can fluoresce to emit light. This singlet state fraction can be increased above the statistically expected 25% if triplet CT states undergo rapid ISC to become singlet CT states. Meanwhile, given the extremely small (≈ 10^-4 eV) spin-orbit coupling in organic molecules, favorable ISC typically requires that the CT states be very nearly degenerate. However, we have observed a nondegenerate CT state gap for the majority of systems and geometries studied. These gaps are not so large that they could not in principle be overcome by unusually large spin-orbit or hyperfine interactions. However, typically the existence of a large gap suggests a slower, activated process is required for intersystem crossing

as compared to the traditional view of ISC arising from purely degenerate mixing of spin states. Thus, in practice, it appears that the most effective means of enhancing the singlet fraction in OLEDs should be the incorporation of some transition metal compound that is capable of increasing k_{ISC}. In fact, this principle has been verified in a recent OLED study [79] where predictions of ΔE_{ST} for the materials involved led to a clear interpretation of previously ambiguous results. The subsequent introduction of a sensitizing agent which selectively enhanced k_{ISC} resulted in an OLED with approximately threefold improvement in fluorescence efficiency. Thus while the strong material dependence of ΔE_{ST} makes back-of-the-envelope predictions difficult the ability to compute these splittings in an *ab initio* manner is still expected to assist in the development of more efficient OLEDs.

2.5 Conclusions

This article outlines the results of some of the first high-level simulations of intermolecular electron-hole pair states in π-conjugated organic semiconducing materials. We find that the CT state singlet-triplet gap exhibits strong material dependence changing in magnitude and even sign depending on the character and relative orientation of the molecules involved. In agreement with reference [102] we find that in cofacial head-to-tail dimers the triplet CT state is favored. However, in nearly all other circumstances we find that singlet CT states are stabilized relative to triplet CT states for small dye molecules and oligomers, and attribute this stabilization to kinetic exchange dominance. Structural relaxation is observed to cause additional stabilization of the singlet CT state, which is ascribed to the increased kinetic exchange that arises as donor approaches acceptor under the influence of Coulombic attraction. High-mobility semiconductors appear to give slightly larger ΔE_{ST}, consistent with the idea that good electronic communication between donor and acceptor enhances kinetic exchange. Furthermore, the calculated magnitude of this gap, on the order of 50 meV for nearest neighbors, can be quite a bit larger than the average gap obtained in experiments, indicating the important role of next-nearest neighbors

and other more distant pairs have on the experimental CT state gap.

These predictions have a direct impact on the design and understanding of OLEDs and the ultimate development of stable, high efficiency blue and green fluorescent materials [52, 79]. However, the chemistry discussed here applies just as well to any organic semiconductors composed of π-conjugated oligomers. Thus, we would expect a similar interplay between singlet and triplet CT states in phthalocyanine dyes and derivitized buckyballs that are often used in organic photovoltaics[108] and in pentacene films that are inocporated into organic transistors [109]. The open questions are how these ideas extend to polymeric systems - where both structural disorder and the formation of *intrachain* CT states will play significant roles in the kinetics - and inorganic/organic hybrid devices - where the delocalized nature of the inorganic carriers could lead to a picuture of singlet and triplet states that involves itinerant, rather than localized, magnetisim. Both of these directions are intensely interesting scientifically and will be the subject of future work.

Another central aim of future work is to find principles for controlling singlet-triplet CT state splittings in π conjugated oligomeric materials. In particular, while not possible with available knowledge, a means for predictably modifying the donor-acceptor orbital overlap is desirable. For example, since ΔE_{ST} also has an important role in organic photovoltaics, where it is desirable for the triplet CT state to lie below the singlet CT state [108] so that recombination is *inhibited*, such control could also lead to more efficient and robust solar cells. In addition, a quantitative understanding of Marcus parameters for donor-acceptor pairs, including driving force, reorganization energy, and coupling could also lead to greater control of OLED efficiency. Methodology for obtaining these parameters from C-DFT has been previously derived [42, 43] and the application of these techniques to organic materials such as those discussed here is actively being pursued. Rates of charge recombination could then be predicted in a first principles manner, for example, leading to a more thorough understanding of whether it is ΔE_{ST} or ΔG that causes the singlet/triplet ratio to deviate from 1:3.

2.6 Acknowledgements

The work in this chapter was performed in collaboration with David Beljonne, who was an author on Ref. [110].

Chapter 3

Extrafluorescence: Including a sensitizing molecule in OLEDs results in enhanced singlet charge recombination

In Chapter 2, we found that the singlet CT state energy is nearly always 10-100 meV below the triplet CT state energy (Table 2.2), strongly suggesting that intersystem crossing (ISC) between these states is unfavorable. We also observed that the splitting between these CT states is strongly dependent on material and spatial orientation (Fig. 2-4). Prior to this finding and in the nearly complete absence of experimental data on the singlet-triplet CT energy splitting, it was commonly assumed that the singlet and triplet CT states were nearly degenerate and that ISC was favorable. However, this assumuption led to difficulties in explaining the observed wide variation in organic light emitting device (OLED) energy efficiency. By establishing that ISC is unfavorable in the absence of spin-orbit coupling, alternative strategies for rationally improving OLED efficiency could be explored. In this chapter, we discuss how modifying the spin-orbit coupling though the insertion of a heavy metal sensitizing agent led to the fabrication of exceptionally efficient organic light emitting devices

(OLEDs).

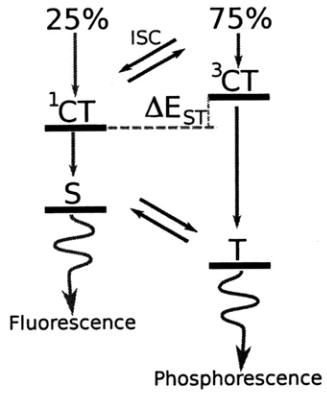

Figure 3-1: Role of singlet-triplet CT state ISC in OLEDs. Triplet CT states are formed three times as often as singlet CT states by randomized combination of injected electrons and holes. If ISC is unfavorable, only 25% of the injected charge pairs recombine to form singlet excitons that lead to fluorescence, while the other 75% of the charge pairs form triplet excitons that undergo slow phosphoresence. Efficient OLEDs maximize the fraction of charge pairs that lead to fluorescence.

3.1 Results

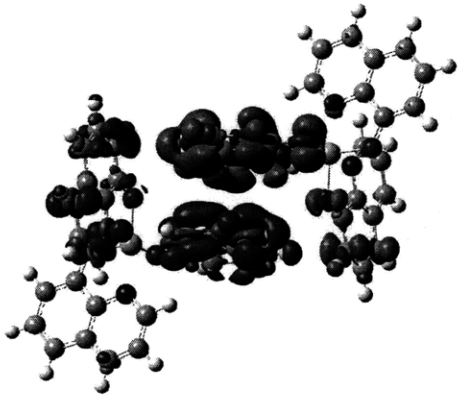

Figure 3-2: Calculated difference between CT and ground state electron densities for δ-Alq_3. Gold (purple) regions are where the CT state contains more (fewer) electrons than the ground state.

To study the effects of spin-orbit coupling on OLED energy efficiency, OLEDs containing an emissive layer of tris(8-hydroxyquinoline) aluminum (Alq_3, Fig. 3-2) doped with either platinum octaethylporhyrin (PtOEP) or metal-free OEP were

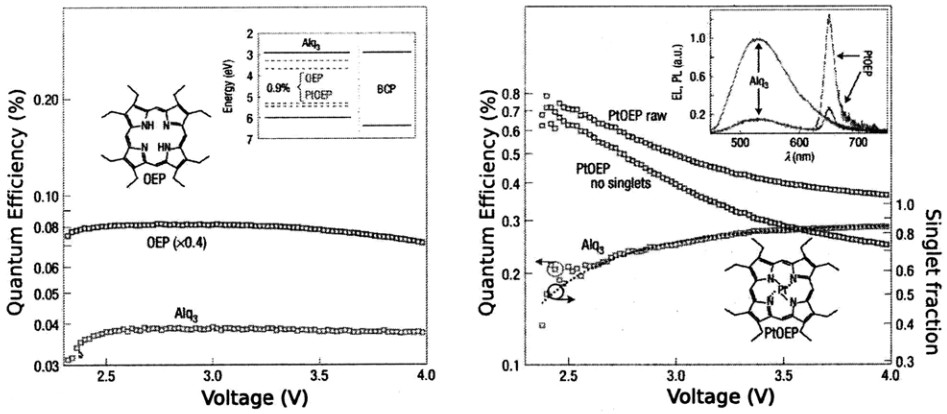

Figure 3-3: Quantum efficiency as a function of voltage (in volts) for an Alq_3/BCP OLED doped by OEP (left pane) and PtOEP (right pane). In the absence of the heavy metal Pt, the quantum efficiencies remain nearly constant with respect to voltage. Meanwhile, insertion of Pt leads to votage-dependent quantum efficiency. PtOEP "no singlets" ("raw") quantum efficiencies are corrected (not corrected) for the contribution from Alq_3 singlets. Left pane inset: Band energies of Alq_3 and BCP. Right pane inset: Photoluminescent spectra (solid lines) for Alq_3 doped with 0.9% PtOEP and for a neat film of Alq_3 shows that the ratio of PtOEP emission to Alq_3 emission is 0.5 ± 0.1.

constructed. The metal-free OEP device serves as a control to isolate the effects due to spin-orbit coupling by the platinum. Table 2.2 shows appreciable splitting between the singlet and triplet CT states of Alq_3, so that ISC is expected to be unfavorable in the absence of spin-orbit coupling. Fig. 3-3 shows the quantum efficiencies of the devices as a function of voltage. It is found that doping with PtOEP leads to voltage dependency that is absent in the Pt-free material.

The singlet fraction χ_s is related to the PtOEP EL (PL) quantum efficiency η^{EL}_{PtOEP} (η^{PL}_{PtOEP}), fraction of electrically excited excitons d_{EL}, fraction of singlet (triplet) excitons transferred to the porphyrin from Alq_3 r_S (r_T) by the equation $\eta^{EL}_{PtOEP} = \eta^{PL}_{PtOEP}\left[(1-d_{EL})\left[(1-\chi_S)\,r_T + r_S\chi_S\right] + d_{EL}\right]$. Similarly, for the Alq_3 quantum efficiency, $\eta^{EL}_{Alq_3} = \eta^{PL}_{Alq_3}\left[(1-d_{EL})\,(1-r_S)\,\chi_S\right]$. To study the change in χ_S, contributions to PtOEP emission due to r_S and d_{EL} are removed through a PL measurement of a 0.9% PtOEP:Alq_3 thin film (Fig. 3-3 right pane inset). Define $f = \frac{\eta^{PL}_{PtOEP}}{\eta^{PL}_{Alq_3}}$. From the thin film PL measurement, $f = 0.5 \pm 0.1$. Then $f = \left[(1-d_{PL})\,r_S + d_{PL}\right]\eta^{PL}_{PtOEP} / \left[(1-r_S)\,(1-d_{PL})\,\eta^{PL}_{Alq_3}\right]$, where d_{PL} is the fraction of optically excited excitons that form on PtOEP. Defining $P = log\left(\eta^{EL}_{PtOEP} - f\eta^{EL}_{Alq_3}\right)$,

$F = log\left(\eta_{Alq_3}^{EL}\right)$, and $A = \frac{[r_T + d_{EL}/(1-d_{EL})]}{[r_T + d_{PL}/(1-d_{PL})]}$, we arrive at an expression for the singlet exciton fraction (Eq. 3.1).

$$\chi_S = -A^{\frac{dP}{dF}}/_{\left(1-\frac{dP}{dF}\right)} \tag{3.1}$$

Absorption strengths of Alq_3 and PtOEP at the laser pump wavelength allows an estimation of $d_{PL} = 6\%$. Therefore, $A > 1$ independently of d_{EL}. The right pane of Fig. 3-3 shows the calculated value of χ_S with $A = 1$. We observe that this singlet fraction coincides with the Alq_3 quantum efficiency. Therefore, we conclude that the voltage dependency of the Alq_3 fluorescence efficiency is a result of the changing χ_S. Furthermore, this dependency coincides with the energies of the Alq_3 triplet (2.05 eV) and singlet (2.7 eV), [111, 112] so we find that the injected charge pairs are excited thermally to form the singlet exciton in the range $V_T < V < V_S$.

Furthermore, the voltage independent quantum efficiency in Fig. 3-3 shows that both the fraction of singlet excitons and the total fraction of electrically excited electrons that form on OEP are independent of voltage, but that doping with PtOEP allows the fraction of singlet excitons to increase with voltage. In fact, at 4 V, the singlet exciton fraction for the PtOEP doped material is found to be 0.84 ± 0.03, which much larger than both the maximum fraction of 0.25 in the absence of ISC or the measured fraction in Alq_3 of 0.20 ± 0.01. [56]

Fig. 3-4 shows the EL efficiency $\eta_{Alq_3}^{EL}$ of Alq_3 as a function of current density and temperature. Using the fact that the EL efficiency difference $\eta_{Alq_3}^{EL} - \eta_{Alq_3}^{EL}|_{T\to 0}$ is proportional to $exp\left(\frac{-|\Delta E_{CT}|}{k_B T}\right)$, [79] it is found that the singlet-triplet CT splitting $\Delta E_{CT} = -7 \pm 3$ eV, where the negative sign indicates that the singlet state lies below the triplet state. The discrepancy in magnitude is a result of the fact that the theoretical result was obtained for nearest-neighbor pairs in a crystal, while the experimental results include significant contributions from long-range interactions in the amorphous experimental bulk.

The results obtained for the PtOEP-doped Alq_3 OLED show that spin-orbit coupling can significantly enhance the fraction of singlet exciton states generated. How-

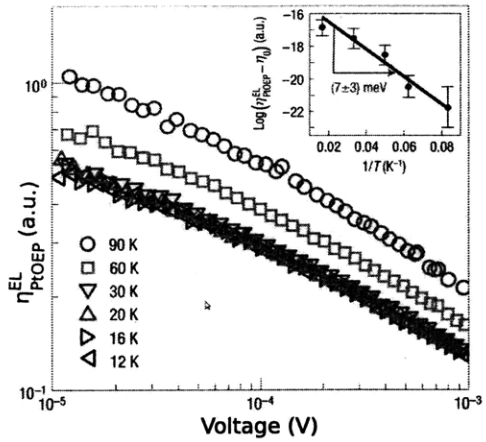

Figure 3-4: Alq_3 EL efficiency η^{EL}_{PTOEP} as a function of current density (A cm^{-2}) and temperature shows that EL efficiency increases as the temperature increases. Inset: An Arrhenius plot shows that phosphoresence is thermally activated. An experimental estimate to the Alq_3 singlet-triplet CT state energy splitting of -7 ± 3 meV is obtained from the Arrhenius plot slope. This result agrees in sign with the theoretical results of $\Delta E_{CT} = -70$ meV for δ-Alq_3 and $\Delta E_{CT} = -25$ meV for α-Alq_3. Here the efficiency is zeroed with $\eta_0 = \eta^{EL}_{PTOEP}|_{T \to 0}$.

ever, fluoresence enhancement was not observed for this device because the singlets are quenched by the PtOEP or are subsequently converted to triplet states. That is, a successful dopant for increasing fluresence must introduce spin-orbit coupling to allow CT state mixing, but must not also allow the singlet and triplet excitons to mix. Figure 3-5 shows a second type of OLED that was fabricated to achieve this selective mixing. The results show that when spin-orbit coupling is introduced by doping the red dye DCM2 with iridium(III) bis[(4,6-difluorophenyl)pyridinato-N,$C^{2'}$] picolinate (FIrpic), a 2.8-fold enhancement, or extrafluorescence) in quantum efficiency compared to an iridium-free control is obtained. The relevant CT state in this device is $FIrpic^-/DCM2^+$, which is shown using constrained DFT calculations to have a large singlet-triplet CT state splitting. That is, in the absence of spin-orbit coupling this OLED should have a maximum quantum efficiency of 0.25.

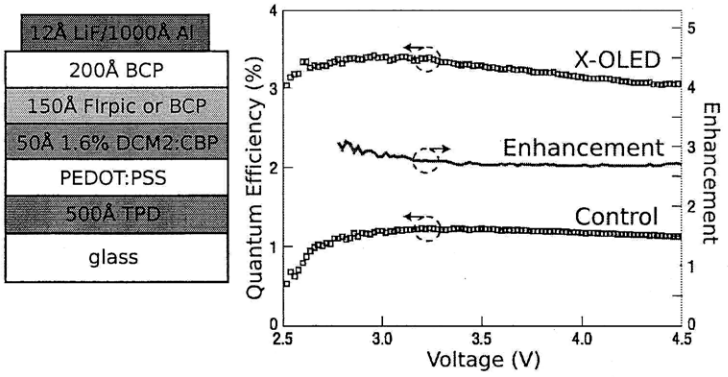

Figure 3-5: The layers of an extrafluorescent OLED (left pane) and quantum efficiency and enhancement for this device and its controls as a function of voltage in volts (right pane).

3.2 Conclusions

Using constrained DFT calculations, we have shown that the singlet CT state energy almost always lies appreciably below the triplet CT state energy and that the difference between these states is highly material and geometry dependent. As a consequence, ISC between these singlet and triplet CT states is expected to be negligible if spin-orbit coupling is absent, and thereby limit the quantum efficiency of an OLED to 0.25. The experimental results summarized here show that spin-orbital coupling introduced via a heavy metal such as Pt or Ir can cause the generated fraction of singlet excitons to far exceed the 0.25 limit. To generate increased fluorescence, it is not sufficient to merely introduce spin-orbit coupling. The newly-formed singlet excitons must be prevented from mixing with triplet excitons. Such mixing control can be obtained by careful choice of material and device architecture.

3.3 Acknowledgements

The experimental work in this chapter was performed by Michael Segal, M. Singh, Kelley Rivoire, and Marc Baldo, who are authors on Ref. [79].

Chapter 4

Electronic Properties of Disordered Organic Semiconductors via QM/MM Simulations

4.1 Introduction

The study of organic electronics presents a new landscape upon which chemists, material scientists, and others are working to reproduce and supplement conventional inorganic semiconductor devices with a palette of small molecule and polymeric materials.[113] These are typically π-conjugated systems with low-lying excited states and the ability to transport both holes and electrons.[9] While work remains to be done, significant progress has been made on device applications such as organic light-emitting diodes (OLEDs),photovoltaics (OPVs),and field-effect transistors (OFETs).[114]

Although monocrystalline organic materials can be produced, most applications are limited by cost to polycrystalline or amorphous structures. Thus disorder greatly affects carrier mobilities and generation-recombination behavior of OSC devices. In addition, because there are no intermolecular covalent bonds, weak van der Waals (vdW) forces dominate interactions in the solid[114] creating localized (Frenkel type)

excitons while strong electron-phonon interactions lead to polaron formation and hopping-type transport. For the computational scientist, the conceptual simplicity of bands in traditional semiconductors has been replaced by a complex disordered system where electron interactions and electron-phonon coupling determine the energy landscape.[9]

Describing OSC electronic properties and transport behavior can be formulated[9, 115] in terms of Marcus ET theory.[116] The electronic states of OSCs can be described with semi-empirical[117], density functional theory (DFT),[115, 118] or wavefunction-based methods.[119] To describe short-range disorder in the solid, simulated annealing can generate dimer structures for which the electronic coupling between pairs of molecules can be computed, leading to an estimate of carrier mobility.[120] To crudely address electrostatic effects of the environment, polarizable continuum models (PCMs) can also be invoked.[121]

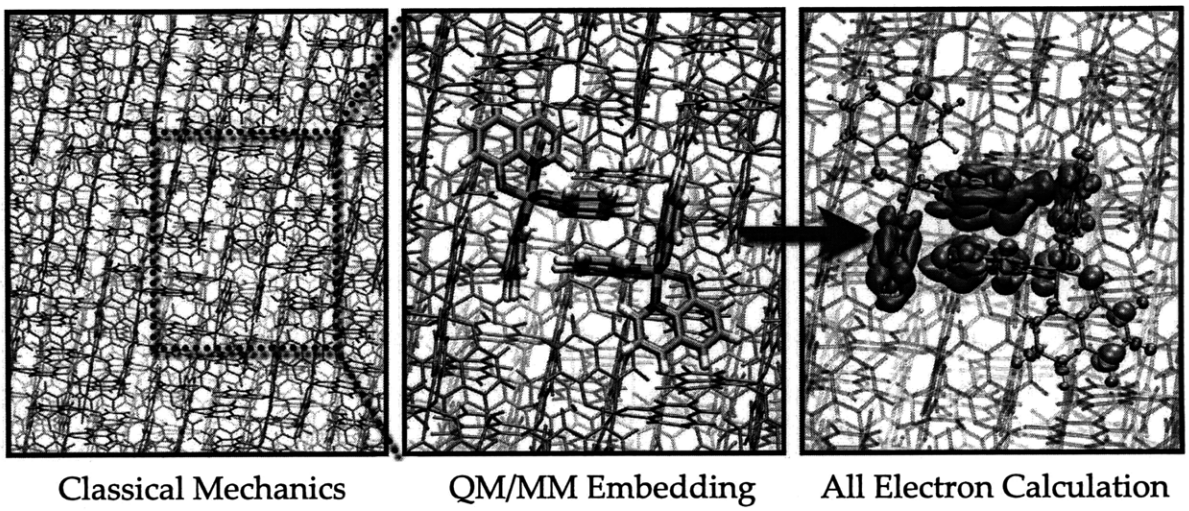

Figure 4-1: Illustration of QM/MM method. Left: Disordered Alq_3 supercell, generated using MM simulation techniques. Center: Selection of QM region within the MM environment. Right: Electronic structure calculation of desired electronic state.

QM/MM studies[122] can shed more light on the impact of the environment on transport properties. By explicitly including intermolecular interactions in the QM/MM potential, the effect of neighboring molecules on optical and transport properties can be better described. Even for an amorphous material with nanometer-scale

disorder, the localized nature of the electronic state means that the QM region need only include one or two monomers (See 4-1). This makes QM/MM calculations vastly faster than a full DFT calculation on the same system.

Recently, we and others[123, 120] have begun a systematic study of organic materials with QM/MM methods. This review is a tutorial intended to illustrate the fundamental principles involved in this new class of simulations. We begin by introducing the relevant theoretical ingredients - the Marcus picture of ET, identifying diabatic states using CDFT, and the integration with QM/MM techniques. To illustrate how the techniques interface with one another, we focus on Alq_3, a well-studied molecule[124, 125, 121, 120, 110] that is the prototypical OLED material.We apply the QM/MM methodology to Alq_3 and compute a range of electronic properties: transport gap, electron- and hole- transfer rates, spectral densities and charge carrier recombination rates. At every stage, we observe the crucial influence of the environment, and particularly disorder, on the distribution of electronic states. We conclude by summarizing the strengths and weaknesses of this approach for studying OSCs and detail future work necessary for broader applications.

4.2 Theory

4.2.1 Marcus Theory of Electron Transfer

In the condensed phase, ET occurs as the static and dynamic polarization of the environment stabilizes (or destabilizes) charged species. For nonadiabatic reactions (see 4-2) this is described by two parameters. Structural fluctuations contribute to the reorganization energy λ, which describes the relaxation of the entire system as a result of the new electronic state. This is balanced by ΔG, the free energy change during ET. The intramolecular ET rate, k_{ET}, can be aproximately written as[116]

$$k_{ET} = \frac{2\pi}{\hbar}|V_{RP}|^2 \frac{1}{\sqrt{4\pi\lambda k_B T}} \exp\left(\frac{-(\lambda + \Delta G)^2}{4\lambda k_B T}\right). \tag{4.1}$$

Here, the prefactor involves the electronic coupling element, V_{RP}, between the (diabatic) reactant and product states of ET.

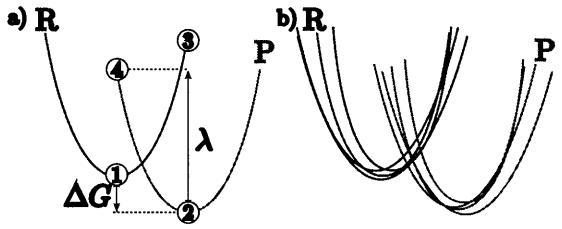

Figure 4-2: Marcus free energies describing an exoergic transition from reactant (R) to product (P) states. **a)** Circles indicate calculations for four-point determination of λ,ΔG. **b)** Within the Marcus picture, static disorder creates a distribution of reactant and product energy landscapes. The horizontal and vertical axes correspond to reaction coordinate and energy, respectively.

As λ is a relaxation energy, it is often written as a sum of an inner-sphere term, λ_i, which comes from the relaxation of the molecules undergoing ET, and an outer-sphere term, λ_o, that describes the relaxation of the environment. Meanwhile, the electronic coupling is $V_{RP} \equiv \langle P|\hat{H}|R\rangle$, where $|R\rangle(|P\rangle)$ is the reactant (product) state, and $\hat{H}$ is the Hamiltonian in the diabatic basis. V_{RP} is often assumed constant along the reaction coordinate (Condon approximation). We will make no such approximations in what follows, but will instead compute V_{RP} at each instantaneous configuration.

We note that Marcus theory is typically an *ensemble* theory. A given reaction is characterized by a single value of ΔG, λ, and V_{RP} (4-2a). Meanwhile, organic solids tend to be disordered, nonequilibrium systems. As a result, an OSC has *many* relevant values of ΔG, λ, and V_{RP} (4-2b) leading to a distribution of ET rates via Eq. 4.1. In order to translate the tangle of energy landscapes in 4-2b into a single rate, one must resolve the individual timescales of relaxation versus charge hopping. In what follows, we will not unravel this particular Gordian knot but instead focus on quantifying the underlying distributions.

4.2.2 Constrained DFT as a Route to Diabatic States

In order to connect the Marcus picture to a physical system, a prescription for diabatic electronic states must be chosen. In this vein, empirical valence bond [122],

semiempirical molecular orbital [117],CDFT[126, 127] and CI-based[128] approaches have all proven useful. In what follows, we employ CDFT to define diabatic electronic states and compute relevant ET parameters. We choose this route because CDFT provides a compromise between computational cost and accuracy: the calculations are fast enough for realistic systems but also reliable enough for chemical accuracy in many properties.

Within CDFT, a diabatic ET state such as D^+A^- is defined to be the lowest energy state such that the partial charges on the atoms that compose the acceptor (A) sum to -1. If the overall system is neutral, the donor (D) atom charges will then sum to $+1$, reflecting the hole left behind by the transferred electron. Other diabatic states, such as $A\ A^-$ or D^+D are defined analogously. The constraint is enforced by applying a local chemical potential bias, V, between donor and acceptor. By varying the strength of this potential, one can control the charge on the acceptor. In CDFT, V is determined *self-consistently* with the charge density to determine the lowest energy state that satisfies the charge constraint exactly [129]. The charge-constrained states thus obtained form the foundation for a seamless connection between DFT and ET theory[126, 130].

For a rigid system like an organic crystal, the entropic contributions to the Marcus parameters (ΔG, λ) are expected to be small, so the task reduces to computing enthalpies. These enthalpies can be computed from a combination of geometry optimizations and energy evaluations. Adopting a notation of $(X|Y)$ for the energy of state X at the optimized geometry of Y, we can compute the driving force and reorganization of $R \rightarrow P$ from (see 4-2)

$$\Delta G \equiv \frac{1}{2}[(R|R) + (R|P) - (P|P) - (P|R)], \tag{4.2}$$

$$\lambda \equiv -\frac{1}{2}[(R|R) - (R|P) + (P|P) - (P|R)]. \tag{4.3}$$

These expressions make the standard linear response assumption that both free energy surfaces are perfect parabolas with the same curvature.[116] Finally, we compute V_{RP} in CDFT using the method of Ref. [131]. There it is noted that the coupling can be

computed from a combination of the overlap between electronic states and the matrix elements of the chemical potential between them:

$$V_{RP} = \langle \Psi_R | \hat{H} | \Psi_P \rangle = \frac{F_R + F_P}{2} \langle \Psi_R | \Psi_P \rangle - \frac{1}{2} \langle \Psi_R | V_R + V_P | \Psi_P \rangle, \tag{4.4}$$

where F_i is the free energy of the i^{th} state and V_i is the constraining chemical potential for that state. Recent applications have shown that CDFT can provide accurate predictions of ΔG, λ, and V_{RP} when used within this framework [126, 127, 130].

4.2.3 QM/MM Modeling of Disordered Systems

QM/MM techniques have a long history of application to systems where a small active site is surrounded by a much larger environment. The simulation cell is thus divided into classical (MM) and quantum (QM) regions, which interact via a QM/MM Hamiltonian.[122] The important quantum phenomena are contained within the molecules of the QM region, while the surrounding MM region provides essential corrections (e.g. local electric fields) from the heterogeneous environment.

The total energy of the QM/MM simulation is given by:

$$E = E_{\text{QM}}(\mathbf{r}_{\text{Q}}) + E_{\text{MM}}(\mathbf{r}_{\text{M}}) + E_{\text{QM/MM}}(\mathbf{r}_{\text{Q}}, \mathbf{r}_{\text{M}}). \tag{4.5}$$

Here, E_{QM} and E_{MM} are the energies of the QM and MM regions, which depend on the coordinates of the QM ($\mathbf{r}_{\text{Q}}$) and MM ($\mathbf{r}_{\text{M}}$) nuclei respectively. $E_{\text{QM/MM}}$ represents the interaction energy between the regions and consists of electrostatic interactions plus an empirical vdW repulsion:

$$E_{\text{QM/MM}} = -\int \sum_{i \in \text{M}} \frac{q_i}{|\mathbf{r}_i - \mathbf{r}'|} \rho(\mathbf{r}')\, d\mathbf{r}' + \sum_{i \in \text{M}} \sum_{j \in \text{Q}} \frac{q_i Z_j}{|\mathbf{r}_i - \mathbf{r}_j|} + \sum_{i \in \text{M}} \sum_{j \in \text{Q}} V_{\text{vdW}}(\mathbf{r}_i, \mathbf{r}_j). \tag{4.6}$$

The MM region can be described using the standard CHARMM force field (FF)

functional form augmented with Drude polarization:

$$E_{\mathrm{MM}} = E_{\mathrm{CHARMM}} + E_{\mathrm{Drude}}. \tag{4.7}$$

Within the Drude model,[132] mobile charged "Drude particles" carrying charge q_i^{d} are harmonically bonded to selected MM atoms, yielding approximate point dipoles. The Drude model thus adds the following harmonic bonds and electrostatic terms to the FF:

$$E_{\mathrm{Drude}} = \sum_i \frac{1}{2} k_i^{\mathrm{d}} |\mathbf{d}_i - \mathbf{r}_i|^2 + \sum_{i,j} \frac{q_i^{\mathrm{d}} q_j}{|\mathbf{d}_i - \mathbf{r}_j|} + \sum_{i,j} \frac{q_i^{\mathrm{d}} q_j^{\mathrm{d}}}{|\mathbf{d}_i - \mathbf{d}_j|}. \tag{4.8}$$

Electronic polarization is modeled by allowing the Drude particles to respond instantaneously to local electric fields, so that for any given nuclear configuration $\{\mathbf{r}\}$, E_{Drude} is minimized with respect to the positions of the Drude particles. The positions of the Drude particles must be determined self-consistently with the QM charge density, because the electric field experienced by the Drude particles depends on the QM charges and vice versa. The empirical parameters contained in the FF were fitted to reproduce available experimental and *ab initio* data (Supporting Information).

4.2.4 Simulation Procedure

We begin our QM/MM calculations by obtaining thermally sampled configurations of the OSC material. A *pure* MM trajectory with a large number of molecules is simulated at constant temperature, from which we extract a large number of snapshots at fixed time intervals for QM/MM calculations.

Each snapshot contains a disordered supercell of many molecules (4-1, left pane). Because electronic states in OSCs are largely localized, molecules distant from the active region mostly contribute long-range effects that are well described by MM. We invoke QM/MM by selecting a small subset of the snapshot (4-1, center pane), which by physical intuition we assume to contain the interesting quantum effects. Finally, the QM molecules are embedded in the MM simulation and treated using a full QM electronic structure calculation (4-1, right pane); the interaction with the MM system

is replaced by the QM/MM Hamiltonian (Eq. 4.5). The MM atomic charges appear as external point charges in the QM calculation, which affect the QM electronic density.

At the boundary between the regions, QM electron density can localize around nearby MM point charges. however, this is an unphysical error caused by the lack of exchange repulsion in the MM region, which we address by replacing MM point charges with Gaussians: $\rho(r) = \frac{1}{\sigma\sqrt{2\pi}} e^{-\frac{(r-r_0)^2}{2\sigma^2}}$, where the blurring parameter. In this work, we choose $\sigma = 3.5$ Å , approximately half the radius of Alq_3.

Within this framework, the Hellman-Feynman forces on QM and MM atoms alike are given by differentiating the QM/MM Hamiltonian with respect to the nuclear coordinates. When an optimized structure is desired (e.g. when computing λ) these forces are used to minimize the energy of the entire system.

4.3 Computational Details

4.3.1 Alq_3 as a Model Material

Alq_3 is an octahedral coordination complex in which three 8-hydroxyquinoline ligands are bound to a central aluminum atom. Numerous experimental and theoretical studies are available in the literature,[124, 133, 134, 125, 121, 120] making this material an ideal candidate for illustrating the methodology. Alq_3 is known to exist in several different crystalline phases; the experimentally determined[135] unit cell of β-Alq_3 is used here as our initial structure because it most closely resembles that of the amorphous film.[136] We constructed a triclinic supercell of 6x6x6 Alq_3 unit cells (Z=2) containing 432 molecules. For consistency with our QM method, our simulation cell used the equilibrium monomer geometry from a gas-phase B3LYP/3-21G geometry optimization, placed in maximal coincidence with the experimental molecular coordinates (RMSD < 0.1 Å).

4.3.2 MM Sampling and QM/MM Methodology

We performed non-polarizable MM sampling in GROMACS 4.0[137] using the NVT ensemble at 300 K. Full periodic boundary conditions were applied, and Bond lengths were held to DFT-optimized values using the LINCS algorithm.The entire simulation length was 5.0ns, intended to sample typical thermal fluctuations in this material. 500ps was allowed for thermal equilibration, after which snapshots were extracted at 20ps intervals to minimize shot-to-shot correlation. QM/MM calculations were performed with the CHARMM[138]-Q-Chem[82] interface[139]. Where noted, the QM/MM calculations account for electronic polarizability of the MM system through the presence of the Drude particles.

4.3.3 Electronic Structure Calculations

Electronic structure calculations were all performed using the 3-21G basis set at the B3LYP level of theory. To investigate the basis set dependence of each property, we performed selected calculations using the larger cc-pVDZ and aug-cc-pVDZ basis sets. Unless specifically noted, we find negligible basis set dependence (¡5% change) for all of the properties discussed in the text.

In the following sections, we determine most excitation energies using time-dependent DFT (TDDFT)[38], with the exception of CT states, which are obtained with CDFT. Becke weights are used to define electron populations in the CDFT framework with charge and spin constrained together.

4.4 Charge Transport Properties

The motion of charge carriers in OSCs is governed by several material properties. First, the transport gap (also called the band gap) measures the energy difference between free electron and hole carriers. It is formally given by the difference between the ionization potential (IP) and electron affinity (EA), $E_t = \text{IP} - \text{EA}$. In OSCs the band structure is influenced both by the heterogeneity of the system (which gives

rise to a distribution of local IPs and EAs) and the intrinsic band width, which is governed by the electronic coupling V_{RP} (also called the hopping integral). Although OSCs have a band structure, the discussion in Section 4.1 should make it clear that it is not appropriate to discuss charge transport in organic materials in terms of band theory. Instead, carrier mobility ($\mu_{e,h}$) is determined by a Marcus-like rate expression, which is in turn influenced both by energetic disorder and the magnitude of V_{RP}.[9, 115]

4.4.1 Transport Gap

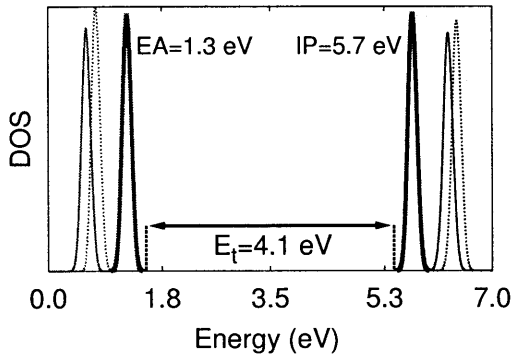

Figure 4-3: Alq_3 electron affinity (EA) and ionization potential (IP) computed with fixed MM point charges (thin solid curves), with only charge blurring (dashed curves), and with only polarization correction (thick solid curves). The transport gap, E_t, is the difference between the IP and EA distribution onsets. All results obtained with 3-21G/B3LYP.

The prescription for computing the transport gap in Alq_3 is straightforward. For a given snapshot, we choose a single monomer and compute QM/MM energies for the cation, anion, and neutral states yielding the transport gap, $E_t = E_+ + E_- - 2E_0$. By computing E_t for different monomers at a variety of snapshots, we can obtain an estimate of the variations in the gap due to disorder.

In 4-3, simulation results for EAs and IPs are presented. At a crude level, we first compute the gap with fixed MM point charges, and obtain an EA (IP) of 0.6 ± 0.05 (6.3 ± 0.06) eV and a transport gap of 5.4 eV (as measured from the IP and EA onsets). Blurring of the MM charges blue-shifts both EA and IP by .15 eV yielding no effect on

E_t. Including polarization corrections in the FF blue-shifts the EA onset to 1.3 ± 0.05 eV and red-shifts the IP onset to 5.7 ± 0.05 eV to give an edge-to-edge transport gap of 4.3 eV. This 1.3 eV polarization correction is a result of the strong interactions of the anion and cation with the charged Drude particles. Indeed, assuming each charge sits in a sphere of radius .7 nm surrounded by a dielectric medium with $\epsilon_s = 2.9$, we obtain ΔE_{pol}=0.68 eV for each charge - very close to the observed polarization shift of 0.55 eV (0.65 eV) for the IP (EA). A small representative set of calculations performed using the aug-cc-pVDZ basis red-shifts the E_t modestly by 0.2 eV. Combining the basis set and polarization corrections gives a corrected estimate of 4.1 eV for the transport gap. Thus we see that disorder has a very small effect on the transport levels of Alq_3: the shot-to-shot variation in IP or EA is only 0.05 eV, and the site to site variation (not shown) is only 0.01-0.02 eV.

A variety of experimental and theoretical results are available for comparison. Experimentally, IPs and EAs of Alq_3 have been determined, yielding band gaps in the range 3.6 - 4.1 eV.[133, 134, 140] Our result is at the higher edge of this range. Previous theoretical studies on Alq_3 monomers within a PCM report an EA (IP) of 1.7 eV (5.8 eV) [121] yielding a transport gap of 4.2 eV. Our results are in excellent agreement with these predictions.

4.4.2 Electronic Coupling

To obtain electronic couplings, we compute the matrix elements ($A \equiv Alq_3$) $\langle A^- A|\hat{H}|AA^-\rangle$ (for electron transport) and $\langle A^+ A|\hat{H}|AA^+\rangle$ (for hole transport). We take the quantum region to be a pair of Alq_3 molecules with an excess electron or hole. Two CDFT states are constructed in which the excess charge is constrained to be on one molecule or the other and the electronic coupling between these states is computed using Eq. 4.4. This is repeated for several near-neighbor pairs at a large number of snapshots. While nuclear heterogeneity has little effect on electron and hole *energies*, it is expected to significantly influence the electron and hole *couplings* because of their strong dependence on relative orientation.

4-4 shows the B3LYP/3-21G electron and hole hopping parameters for several

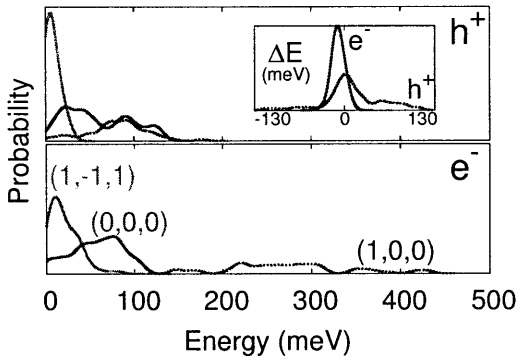

Figure 4-4: Electron (e^-) and hole (h^+) electronic coupling distributions. Inset: The difference, $\Delta E = E_{\text{blur}} - E_{\text{noblur}}$, between blurred and unblurred couplings.

different pairs (indexed by the lattice vector separating them) with fixed MM point charges. The inset shows that while charge blurring can change individual couplings up to 100 meV, the distributions are not significantly shifted. For a given dimer we note the coupling can vary by as much as a factor of five as a function of time - suggesting significant dynamic heterogeneity of the hopping rate on the nanosecond timescale. There is also obvious static structure in the data: despite the width of the distributions, the couplings typically obey $V^h(1,-1,1) < V^h(1,0,0) \approx V^h(0,0,0)$ and $V^e(1,-1,1) < V^e(0,0,0) < V^e(1,0,0)$. Finally, we note that holes tend to have a higher density of very small couplings, while electrons account for most of the high couplings.

These results can be compared to previous theoretical efforts. Lin et al. have shown that electron couplings in the perfect β crystal can be up to 289 meV - ten times as large as the largest hole coupling[136]. Meanwhile Kwiatkowski et al. have shown that in an amorphous sample both electron and hole couplings are in the 0-100 meV range [120]. As our simulations are on a thermalized crystal structure, lying somewhere between the two aforementioned systems, we see that disorder tends to progressively enhance small hole couplings while disrupting some of the strong electron transport pathways in Alq_3.

4.4.3 Reorganization and Mobility

λ^e (λ^h) can be computed by: 1) constraining the electron (hole) to be on one monomer and relaxing the structure of the whole system, 2) repeating the process with the electron (hole) constrained on the opposite monomer, and 3) computing λ as in Eq. 4.3. This process takes tens to hundreds of times longer than an energy calculation, and so it is not computationally feasible to compute λ for every pair of monomers or every snapshot. In order to generate 4.1, we have therefore modeled only a handful of dimers from a single snapshot.

Table 4.1: Calculated Marcus parameters and rates for various donor/acceptor pairs within Alq_3 crystal, labelled by the lattice vector between the monomers. All energies are reported in meV except for ΔG^{CT} (eV). Rates are reported in s^{-1}. Rows are arranged in order of increasing Al-Al separation.

Lattice	Hole Transport				Electron Transport				Recombination		
Vector	λ^h	ΔG^h	V^h	$\log_{10}(k_h)$	λ^e	ΔG^e	V^e	$\log_{10}(k_e)$	λ^{CT}	ΔG^{CT}	V_{RP}
(1,0,1)	333	-38	87	14.0	352	25	115	14.0	653	-3.07	104
(0,-1,0)	245	36	45	13.4	285	-6	45	13.4	498	-3.26	69
(0,0,1)	272	-30	87	14.1	377	38	63	13.4	337	-3.38	119
($\pm$1,0,0)	245	-39	46	13.6	366	-171	33	13.4	614	-3.08	86
(0,0,0)	162	-47	35	13.6	238	-18	86	14.1	457	-3.20	195
(1,-1,0)	272	16	20	12.7	492	9	52	13.1	532	-2.98	196
(1,0,0)	220	-6	94	14.2	253	-17	317	15.2	283	-3.50	159
(0,$\pm$1,0)	210	-86	13	12.7	338	10	80	13.8	364	-3.54	134
(1,-1,1)	157	79	3	11.3	354	-4	4	11.2	225	-3.64	12
(0,-1,1)	173	-3	<1	10.3	373	-10	3	11.1	244	-3.71	N/A
(-1,-1,0)	173	-45	< 1	9.9	337	-62	1	10.3	279	-3.75	N/A

As shown in 4.1, the typical electron (hole) reorganization energy in Alq_3 is 337 $\pm$ 63 meV (223 $\pm$ 47 meV). These values are significantly larger than the typical V_{RP}, consistent with the generally poor transport properties (and high reorganization barriers) of organic materials. Meanwhile, the distribution of ΔG ($\pm$ 48 meV) is consistent with the width of the IP and EA distributions in 4-3.

We can further estimate λ_i by performing a gas-phase calculation to find λ_i^e=216 meV and λ_i^h=208 meV so that $\lambda_o^e \approx 111$ meV while $\lambda_o^h \approx 15$ meV. Thus, the reor-

ganization energy for electrons is larger primarily because the *environment* traps an excess electron more strongly than an excess hole. This effect can be rationalized by noting that the electron wavefunction is typically more delocalized and therefore more susceptible to environmental fluctuations.

As illustrated in 4.1, with λ, ΔG, and V_{RP} for a given pair, we can predict the rate of ET via Eq. 4.1, and we note that in 8 of 11 cases the rate of ET is larger than those for hole transfer. The primary differentiating factor is that the typical hopping integral for electrons is considerably larger than for holes. In most cases, this is enough to overcome the difference in activation barriers, which typically favors holes. Our finding agrees qualitatively with the experimental observation that Alq_3 is a good electron transport material, with $\mu_e \approx 100\mu_h$. Because of heterogeneity in k_e and k_h, it is not a trivial matter to make a quantitative prediction of the mobility based on these rates. Since μ is most sensitive to the slow, rate limiting values of k, one must simulate carrier diffusion using the given hopping rates to obtain mobilities [120]. Such a simulation is beyond the scope of this tutorial, but the feasibility of such mesoscopic simulations provides the final link between atomistic data and bulk properties.

4.5 Optical Properties

The optical response of Alq_3 is dominated by two Frenkel-type excitons: a singlet state that fluoresces in the green and a triplet that phosphoresces in the red. However, the activity of Alq_3 in OLEDs also depends critically on the distribution of CT excitons, which are intermediates in the process of electron-hole recombination. In contrast with transport properties that describe ground state behavior, optical properties pertain to excited states making them somewhat more challenging from a simulation perspective. In what follows, we focus on just two features: the spectral densities of the various states and the rate of CT recombination to the ground state.

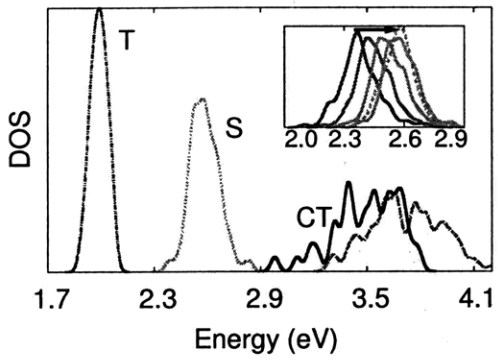

Figure 4-5: Triplet (T), singlet (S), and CT exciton spectral densities. Solid CT curve includes polarization correction. Inset: Dependence of singlet exciton states on blurring. The arrow indicates increasing σ, from 0 (no blur) to ∞ (no charges). The other states are insensitive to σ

4.5.1 Spectral Density

To generate singlet and triplet exciton spectral densities, the quantum region of the QM/MM system was chosen to be a single monomer, and TDDFT was used to obtain the lowest lying singlet and triplet states at a variety of snapshots. For CT excitons, a $(0,0,0)$ dimer pair was chosen as the quantum region and intermolecular CT energies were computed as the difference between the CDFT A^+A^- and AA state energies for each geometry snapshot. The resulting spectral densities are presented in 4-5.

4-5 shows singlet excitons centered at 2.6 ± 0.08eV , triplet excitons at 2.0 ± 0.04 eV and CT state energies at 3.7 ± 0.2 eV (all with charge blurring). Thus we see immediately that exciton and CT energies are more sensitive to disorder than either IP or EA. As a result, diffusion of these states will be more strongly influenced by energetic trapping than was the case for charge transport, where fluctuations in the hopping parameter dominated the mobility. The singlet and triplet exciton results can be compared to a range of experimental and theoretical studies. Optical absorbance studies place the singlet exciton at 2.7 eV [141], while a gas-phase TDDFT calculation finds an exciton energy of 2.8 eV.[142] For the triplet, phosphorescence studies find energies of 2.03-2.10 eV [143, 111, 144] while gas-phase calculations report 2.1 eV. Our exciton energies are thus fairly consistent with the existing data and suggest only a very small environmental effect on the Frenkel-type exciton energies.

One important point is that while triplet and CT excitons are insensitive to blurring (as all properties discussed so far have been) the singlet is quite sensitive to blurring (4-5,inset). The average singlet energy shifts by 0.3 eV as σ is increased from zero (point MM charges) to infinity (no MM charges). For the value of σ=3.5 Åused here, there is only a small (<0.1 eV) difference between the QM/MM and pure QM calculations for the singlet, which is physically realistic.

Little is known experimentally about the CT states, so that calculations like the ones presented here are the primary source of information about these intermediates. 4-5 includes the distribution of CT energies both with and without polarization; polarization shifts the average CT energy by 0.2 eV and clearly increases the density of deeply trapped CT states (i.e. states ¿1 eV below the band edge). These deeply trapped states could play an important role in OLEDs, facilitating the formation of singlet excitons (which are very close in energy to the deeply trapped CT states) while avoiding the triplet states (which remain well-separated from the CT states)[65].

4.5.2 Electronic Coupling

To predict the electronic coupling between the neutral ground state and CT exciton, we need to compute the matrix element $\langle A^+A^-|\hat{H}|AA\rangle$ using Eq. 4.4. As previously, we model heterogeneity by computing V_{RP} for multiple geometry snapshots sampled from the MM trajectory. 4-6 shows the resulting CT electronic coupling for the (0,0,0) dimer using 3-21G. While the distribution is broad, we note that these CT couplings are 2-3 times larger than the typical electron and hole couplings in 4-4, reflecting the fact that in the CT state the electron and hole attract one another, leading to larger overlap.

We consider two corrections to the results in 4-6. We see that blurring somewhat narrows, but does not shift, the distribution. Further, applying the polarizable FF is expected to have only a small effect on V_{RP}, which primarily involves the reactant and product wavefunctions, not their energies. Thus our results suggest that the CT-to-ground coupling is significantly larger than the electron or hole coupling, tending to increase the charge recombination rate.

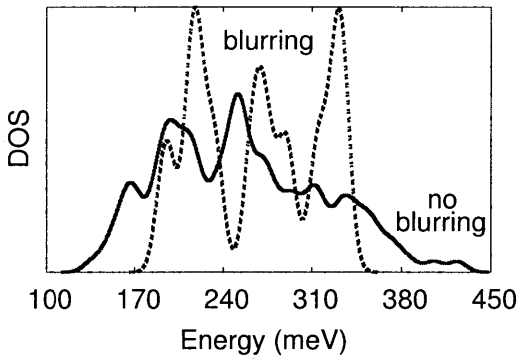

Figure 4-6: CT-ground state state electronic coupling densities. The dashed (solid) density curve is computed with (without) MM charge blurring.

4.5.3 Charge-Transfer Reorganization

Just as for charge transport, there is a λ associated with the formation of a localized CT state. However, while charge transport typically occurs in the normal regime ($\Delta G < \lambda$), the inverted regime ($\Delta G > \lambda$) is relevant for CT states. Thus, while small values of λ speed up transport, they *slow* charge recombination. To evaluate the significance of this, we compute the CT reorganization energy for a number of snapshots using Eq. 4.3 with $R = A^+A^-$ and $P = A\ A$ (4.1).

We find $\lambda^{CT} = 384 \pm 133$ meV. If the monomers did not interact, we would expect λ^{CT} to be the average of electron and hole reorganization energies: $\frac{1}{2}(\lambda^e + \lambda^h) = 315$ meV. However, the dimers here are nearest-neighbors so that a significant portion of the relaxation energy comes from the two monomers approaching each other in the relaxed A^+A^- structure, improving the attractive Coulomb interaction and increasing λ_i^{CT} relative to the isolated monomers' value. We find that the pairs with the largest λ^{CT} also tend to have the smallest Al-Al separations, further supporting this conclusion.

Finally, with the Marcus parameters in hand for several pairs, we can predict the rate of charge recombination to the ground state (k_{cr}) using Eq. 4.1. The results in 4.1 yield extremely slow rates, with a typical CT lifetime of $\gg 1$ s. This long lifetime is primarily due to the large disparity between ΔG (≈ 3.5 eV) and λ^{CT} ($\approx$

.4 eV) leading to extremely slow rates in the inverted regime. Thus, direct charge recombination to the ground state is not likely to be a significant loss mechanism for Alq_3 in OLED applications, where the rate of exciton formation will be many orders of magnitude faster than these recombination rates.

4.6 Conclusions

In this tutorial, we have demonstrated how simulation can be used as a tool to study disordered OSCs. Taking Alq_3 as a prototypical example, we have shown how to compute its electronic properties within a complex, heterogeneous environment. Our results are in good agreement with existing experimental findings, and reinforce the idea that while exciton transport in Alq_3 may be limited by energetic disorder, charge transport is limited by fluctuations in electronic coupling.

The basis of our investigation is a synthesis of tools that together provide an efficient means of computing accurate electronic properties in a large, disordered system. The primary approximation is the assumption that the electronic states are localized, which is a necessary component for the QM/MM decomposition. This is not generally valid in inorganic devices but is thought to hold quite generally in OSCs, where Anderson localization dominates the energy landscape.

Moving forward, a number of extensions of the present work should be explored. Most importantly, to make simulations of this type into a predictive tool, these ideas should be applied to a wider array of OSC systems. Here we demonstrate the techniques on a single material while carefully testing sensitivity to the computational parameters. Similar calculations for the alphabet soup of popular OSC materials - C_{60}, TPD, P3HT, CuPc ... - will lead to a recipe of simulation parameters most accurate for a range of systems. Guidelines of this sort are crucial in addressing technologically relevant structures, such as donor-acceptor interfaces and bulk heterojunctions.

On a technical level, the weakest step in our methodology is clearly the process of MM sampling. We use a single, long MM trajectory to sample the configuration space.

Because these materials are glassy, better phase space sampling could be obtained either from Monte Carlo or parallel tempering simulations. Further, it is not entirely clear that MM provides an adequate picture of the energy landscape. In this respect, it may prove interesting to explore the influence that a full QM/MM trajectory would have on the results.

The methodology presented above can be further extended to explore an even wider range of essential material properties. Here, we have not computed any charge carrier mobilities, but a prediction of this type is within reach by employing our calculated rates in kinetic Monte Carlo simulations [120]. Alternatively, although the present tutorial has focused on parameters governing charge transfer, analogous simulations of exciton transfer could reaveal exciton diffusion lengths in disordered materials. All of the above applications would require some enhancement of our existing computational machinery, but would augment our ability to understand and predict the properties of OSCs.

4.7 Acknowledgements

The work in this chapter was done in collaboration with Lee-Ping Wang, Sina Yeganeh, and Shane Yost SD thanks Ben Kaduk for assistance with the CDFT coupling code.

Chapter 5

Exciton/Charge-transfer Electronic Couplings in Organic Semiconductors

5.1 Introduction

Organic semiconductors (OSCs) hold promise as low-cost solar cells [145, 146, 147, 148, 149, 150, 151, 152] and as versatile, flexible, high-contrast display technologies [153, 154, 155, 156, 157] that are amenable to cost-effective large-scale production. Several of the challenges to improving the energy conversion efficiencies of these devices include maximizing absorption (or emission) efficiencies, electron and hole transport, and charge collection (or charge recombination). [158, 159] A detailed understanding of how these device properties are related to OSC materials and device architecture is important for guiding the design of semiconductor technologies. In this present study, we look closely at electronic couplings, which play an important role in providing this detailed understanding.

Spatially localized excitons and spatially delocalized CT states play crucial roles in OSCs. Fig. 5-1 illustrates the interplay of these states at a PV heterojunction interface. In this figure, the heterojunction is composed of OSC materials A and

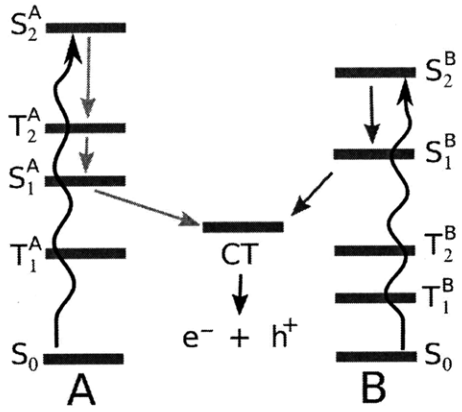

Figure 5-1: Cartoon of two possible electron transfer pathways through an organic photovoltaic material. The spatial location (molecule A or B) of the localized excitons is denoted by superscript. The CT state is delocalized over both molecules.

B. The first several localized singlet and triplet excitons are presented for each PV material where the molecular location of the exitation is labeled by superscript. A delocalized CT state that involves both A and B is also shown. In the first step of the solar cell's operation cycle, the A-B dimer is photoexcited to a singlet excitonic state localized on either A or B. After some time, the system can undergo a series of relaxations from one exitonic state to another exitonic state and eventually relax to the CT state. Finally, the CT state can undergo charge separation to form free electron and hole charge carriers. [160] These charge carriers can drift toward the electrodes and produce the desired current. Given the various electronic states involved in this multistep relaxation process, there are many possible relaxation pathways that the system may follow. In Fig. 5-1, the red and green arrows represent two concievable pathways leading from photoexcitation to charge dissociation. The transition rate of each multistep process is not faster than its constituent steps. Furthermore, some of the possible process can be act as energy loss mechanisms that reduce the fraction of incident light on the devices that is converted into electricity. In optimizing these devices, we wish to choose materials and device morphologies that maximize the rate of desirable relaxation mechanisms while minimizing loss mechanism rates. [158] A useful tool for comparing electronic transistion rates between states a and b is the Marcus rate expression (Eq. 5.1).

$$k_{ab} = \frac{2\pi}{\hbar}|H_{ab}|^2 \frac{1}{\sqrt{4\pi\lambda k_B T}} exp\left(\frac{-(\lambda + \Delta G^o)^2}{4\lambda k_B T}\right) \tag{5.1}$$

Here, ΔG^o is the driving force, λ is the reorganization energy and $H_{ab} = \langle\psi_a|H|\psi_b\rangle$ is the coupling between states described by the wavefunctions ψ_a and ψ_b and electronic Hamiltonian H. Importantly, we note that the rate is proportional to the square modulus of the coupling.

We have seen that predicting the rates of electronic transistions within OSCs is crucial for designing superior OSCs. Conceptually understanding the mechanisms governing these electronic transitions is also paramount and will be the primary focus of this paper. To begin this conceptual discussion, it is convenient to describe electronic energy surfaces as either being diabatic or adiabatic. Given non-orthonormal diabatic states H_{aa} and H_{bb} and the coupling between these states H_{ab}, a generalized eigenvalue problem (Eq. 5.2) can be solved to obtain the corresponding adiabatic states $\Psi^{\pm}$ and energy surfaces $\varepsilon^{\pm}$.

$$\begin{pmatrix} H_{aa} & H_{ab} \\ H_{ba} & H_{bb} \end{pmatrix} |\Phi^{\pm}_{ad}\rangle = \varepsilon^{\pm}_{ad} \begin{pmatrix} S_{aa} & S_{ab} \\ S_{ba} & S_{bb} \end{pmatrix} |\Phi^{\pm}_{ad}\rangle \tag{5.2}$$

An important distinction between diabatic and adiabatic states is that diabatic states are characterized by uniform electronic character as one moves along an arbitrary nuclear coordinate. Thus, if a state has ionic (covalent) character at one point on its diabatic surface, it will have ionic (covalent) character at every point on that diabatic surface. In contrast, adiabatic states, which result from rigorously applying the Born-Oppenheimer approximation, may have varied electronic character at different points on the same adiabatic energy surface. Another way to conceptualize the difference between diabatic and adiabatic states is that diabatic surfaces can energetically cross each other, while adiabatic surfaces instead undergo an "avoided crossing" near the diabatic crossings (Fig. 5-2).

The interplay between diabatic and adiabatic states is important for understanding electronic transitions. That is, neither diabatic nor adiabatic states can alone

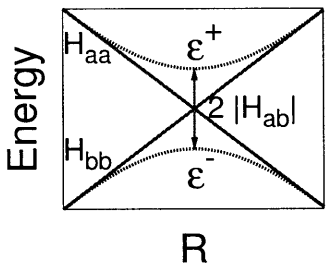

Figure 5-2: Cartoon of adiabatic (dashed curves labeled H_{aa} and H_{bb}) and diabatic states (solid curves labeled $\varepsilon^{\pm}$) at the crossing of the diabatic states as a function of some electronic coordinate R. The coupling H_{ab} is half of the separation between the adiabatic states at the crossing.

describe electronic transitions. For example, suppose in Fig. 5-2 that the system has been excited onto the upper adiabatic energy surface. It is only by transitioning through one of the diabatic states that the system relaxes to the lower adiabatic surface. Furthermore, the relative positions of the diabatic states with respect to the adiabatic states allows us to qualitatively describe the relaxation process. Since such processes are integral to the function of OSCs, we wish to have both the diabatic and adiabatic states.

A variety of methods have been developed for obtaining electronic couplings. In particular, if adiabatic energy surfaces are available, the coupling at the avoided crossing can be identified as one-half of the minimum energy separation between the adiabatic surfaces (Fig. 5-2).[9] For obtaining couplings away from the avoided crossing, Mulliken-Hush methods [161] are often applied, but these methods require experimental spectroscopic data. A number of empirical and semi-empirical approaches for obtaining couplings between various types of electronic states have been developed. [162, 163, 164, 165, 166] In this present study, we present an *ab* initio method for obtaining electronic couplings between CT states generated by constrained DFT (CDFT) [39] and excitons generated by time dependent density functional theory (TDDFT). [167] This effort represents an expansion of previous work that described a method for obtaining electronic couplings between pairs of CDFT states.[43] In addition to being *ab* initio, the approach described in this study takes advantage of

the balance between accuracy and computational tractability that the TDDFT and CDFT methods offer when excited states are desired. After having demonstrated the method's utility for constructing the adiabatic states of two specific and relevant organic dimers, we will briefly discuss implications of our coupling results for OSC electron and hole transport.

5.2 Methods

5.2.1 Linear response TDDFT states

Linear response time independent density function theory (TDDFT) is a successful method for obtaining excited states from ground state DFT densities. [167] Excited states obtained by TDDFT are constructed as linear combinations of singly excited Slater determinants (Eqn. 5.3). In this equation, $\tilde{c}_{ia}$ is the transition amplitude for promoting the electron from occupied state i to virtual state a, σ is the spin associated with the orbital (α or β), and $\Phi_{ia}^{ex,\sigma}$ is the Slater determinant with an electron promoted from the occupied state i to the virtual state a.

$$|\Phi^{ex}\rangle = \sum_{ia} \sum_{\sigma=\alpha,\beta} |\Phi_{ia}^{ex,\sigma}\rangle \tilde{c}_{ia}^{\sigma} \tag{5.3}$$

For the exact density functional, TDDFT states are rigorously adiabatic states because they obey the Born-Oppenheimer approximation. However, for commonly used approximate functionals, we typically observe that the TDDFT states behave as diabatic or diabatic-like states. Although there are both spatially localized and spatially delocalized TDDFT states, these two types of states generally are energetically well separated, which essentially insures they will behave diabatically. Identifying a given TDDFT state as localized or delocalized can be done by attachment/detachment density analysis. [168] If the attachment density is confined to the same molecule as the detachment density, the state is identified as localized to a single molecule. On the other hand, if the attachment density for a TDDFT state is on a different molecule than the detachment density, the TDDFT state is identified as a CT-like delocalized

state. This attachment/detachment analysis can be conducted at several points along a given TDDFT surface to confirm that the electronic character remains consistent from one location on the surface to another. We also note that since excitons are localized on single monomers, exciton energies obtained for dimer systems at large monomer-monomer separations are expected to be essentially the same as exciton energies obtained for a single monomer. Therefore, dimer TDDFT energies that do not correspond to a monomer TDDFT energy are identified as delocalized CT-like states.

5.2.2 Constrained density functional theory (CDFT)

Constrained density functional theory (CDFT) has been shown to be a reliable, inexpensive method for obtaining long-range CT state energies. An important property of CT states obtained by CDFT is that they are represented by a single Slater determinant. The details of this approach have been presented elsewhere [39, 40, 42, 43, 41]. Here, we briefly review CDFT and illustrate the use of this computational tool as it pertains to obtaining electronic couplings.

In the CDFT formalism, we build constraints of the form

$$\sum_{\sigma} \int w_c^{\sigma}(\mathbf{r})\, \rho^{\sigma}(\mathbf{r})\, d\mathbf{r} = N_c \tag{5.4}$$

where the sum is over spins such that $\sigma = \alpha$ or β, c is the constrained region of the system, w_c is a weighting function that corresponds to the constrained property and N_c is the expectation value of the constrained property. Eq. 5.4 is then combined as a Lagrange multiplier constraint with the Kohn-Sham energy functional $E[\rho]$ to generate a new functional

$$W[\rho, \{V_c\}] = E[\rho] + \sum_{c}^{m} V_c \left(\sum_{\sigma} \int w_c^{\sigma}(\mathbf{r})\, \rho^{\sigma}(\mathbf{r})\, d\mathbf{r} - N_c \right), \tag{5.5}$$

where the c^{th} Lagrange multiplier is V_c, and there are m constraints. W is then made stationary with respect to ρ and V_c. By this procedure, we obtain the energy

$E(\rho)$ as a natural function of the expectation value N_c. In the present study of electronic couplings, spin polarized CT states are generated by applying both charge and spin constraints via Eq. 5.4. A charge constraint is applied that forces the donor (acceptor) molecule to have an excess charge of $+1$ (-1). A concurrent constraint on the net spin forces the donor and acceptor, respectively, to have excess spin of $\pm\frac{1}{2}$. Importantly for the present study, applying these constraints produces CT states that are rigorously diabatic.

5.2.3 Electronic couplings between TDDFT and CDFT states

The electronic couplings whose properties are the focus of this study are

$$H_{ab} = \langle \psi_a | H | \psi_b \rangle, \tag{5.6}$$

where ψ_a and ψ_b are the wave functions corresponding to state a and b and H is the electronic Hamiltonian. In particular, we are interested in computing the electronic coupling between CT states obtained by CDFT and excitons obtained by TDDFT. To do this, we adapt the constrained approach that has been successfully demonstrated for obtaining couplings between CT and neutral states. [43]

In the constrained approach to electronic couplings, we use Kohn-Sham orbitals to appoximate the true wavefunction. This allows us to write the coupling matrix element (Eq. 5.6) in terms of a single electronic density. To accomplish this, consider solutions of

$$\left(H + V_c w_c\right) |\Phi_c\rangle = F |\Phi_c\rangle$$

with

$$F = E\left[\rho_c\right] + V_c \int w_c \rho_c = E + V_c N_c.$$

We add and subtract the term $V_c^a w_c$ from the coupling matrix element's operator, and chose Φ^a to be an eigenstate of the operator $H + V_c^a w_c$ with eigenvalue $E + V_c^a N_c$.

Then we obtain

$$H_{ab} = \langle \Phi^a | H | \Phi^b \rangle = \langle \Phi^a | H + V_c^a w_c - V_c^a w_c | \Phi^b \rangle = (E + V_c^a N_c) \langle \Phi^a | \Phi^b \rangle - V_c^a \langle \Phi^a | w_c | \Phi^b \rangle. \tag{5.7}$$

Here, $\langle \Phi^a | \Phi^b \rangle$ is the overlap between states a and b, while $\langle \Phi^a | w_c | \Phi^b \rangle$ is the matrix element of the one-body weight operator. This result is reasonable because it says that the electronic coupling depends on both the magnitude of the orbital overlap and how strongly the weighting operator links the states.

For the true density functional, $\langle \Phi^a | H | \Phi^b \rangle$ is the Hermitian conjugate of $\langle \Phi^b | H | \Phi^a \rangle$. However, we find that

$$H_{ba} = \langle \Phi^b | H | \Phi^a \rangle = \left(E + V_c^b N_c\right) \langle \Phi^b | \Phi^a \rangle - V_c^b \langle \Phi^b | w_c | \Phi^a \rangle,$$

where V_c^b is the constraining potential corresponding to state b. For approximate functionals, $V_c^a \neq V_c^b$, so the Hermiticity condition is not satisfied. To approximately satisfy Hermiticity, we choose the electronic coupling to be the average of H_{ab} and H_{ba}. This average is reasonable because H_{ab} overestimates the electronic coupling when H_{ba} underestimates the coupling, and vice versa.

Eq. 5.7 reduces the problem of computing the coupling to obtaining a zero-body overlap and one-body weight matrix element. Furthermore, both CDFT and TDDFT in which we are interested are expressed in terms of Slater determinants. Therefore, computing the electronic coupling via Eq. 5.7 involves computing zero- and one-body matrix elements of Slater determinants.[169] For each zero- or one-body matrix element evaluation, the computationally demanding step is computing the determinant of an N-rank matrix, where N is the number of electrons in the system. Determinant evaluations have a complexity of order N^3 and each TDDFT state is typically represented as a sum of N^2 Slater determinants (Eq. 5.3), so computing the coupling between a TDDFT and CDFT state Eq. 5.8 involves $O(N^5)$ determinant evaluations. With this complexity scaling, computing the coupling of even medium-sized molecular systems becomes intractable.

$$\langle \Phi^{CT} | \Phi^{ex} \rangle = \sum_{ia} \sum_{\sigma=\alpha,\beta} \langle \Phi^{CT} | \Phi_{ia}^{ex,\sigma} \rangle \tilde{c}_{ia}^{\sigma} \tag{5.8}$$

To decrease the complexity scaling of the coupling calculation, we use a Thouless rotation [170] to re-express the TDDFT excited states as a sum of two Slater determinants. In particular, we define

$$\phi_i(\pm\varepsilon) \equiv \phi_i \pm \varepsilon \sum_a \tilde{c}_i^a \phi_a$$

where ϵ is small, ϕ_i is the ith occupied Kohn-Sham orbital and ϕ_a is the ath virtual Kohn-Sham orbital. That is, we construct new orbitals $\phi_i(\pm\varepsilon)$ that mix small amounts of the virtual orbitals with each the ith occupied orbitals. From these constructed orbitals, we build a pair of Slater determinants $\Phi(\pm\varepsilon)$.

$$\Phi(\pm\varepsilon) \equiv |\phi_1(\pm\varepsilon)\,\phi_2(\pm\varepsilon)\,\phi_3(\pm\varepsilon)\ldots| =$$

$$|\phi_1\phi_2\phi_3\ldots| \pm \varepsilon \sum_{ia} \tilde{c}_i^a \phi_i^a + O\left(\varepsilon^2\right)$$

Using these definitions, the TDDFT state becomes

$$|\Phi^{ex}\rangle = \sum_{ia} \tilde{c}_i^a \Phi_i^a = \lim_{\varepsilon \to 0} \left(\frac{\Phi(+\varepsilon) - \Phi(-\varepsilon)}{2\varepsilon} \right) \tag{5.9}$$

With the TDDFT state expressed in this two determinant form, the matrix element of Eq. 5.8 has the manageable computational complexity of $O(N^3)$.

TDDFT states are generally not orthonormal with CDFT states because they are eigenstates of different Hamiltonians. Therefore, to make the couplings we obtain here comparable to couplings obtained by other methods, we apply an orthonormalizing step. That is, we define $S_{ij} = \langle \Psi^i | S | \Psi^j \rangle$ and weight matrix $w_c^{ij} = \langle \Psi^i | w_c | \Psi^j \rangle$ and solve the generalized eigenvalue problem

$$\begin{pmatrix} w_c^{aa} & w_c^{ab} \\ w_c^{ba} & w_c^{bb} \end{pmatrix} C = n \begin{pmatrix} S_{aa} & S_{ab} \\ S_{ba} & S_{bb} \end{pmatrix} C$$

for eigenstates C and eigenvalues n. The orthonormalized coupling element $\tilde{H}_{ab}$ is then the off-diagonal element of $C^{\dagger}HC$, where H is the Hamiltonian in the non-orthonormalized diabatic basis.

5.2.4 Computational Details

In this paper, we use the 3-21G basis set, B3LYP hybrid density functional, DFT, CDFT, and full linear response TDDFT as implemented in Q-Chem.[82] Becke weights[83] are used in the constrained population analysis. Attachment/detachment analysis[168] is used to obtain the electronic spatial character of the TDDFT states.

Diabatic energy surfaces for the chosen dimers are produced by making the monomer planes coincident, scanning along the separation distance between the monomer planes, and obtaining TDDFT and CDFT states for each separation distance. For the heteodimers studied, the CDFT constraints were chosen to obtain the lowest energy CT state.

5.3 Results

5.3.1 Triphenylene:1,3,5-trinitrobenzene

As a first illustration of the TDDFT/CDFT coupling method, we chose a dimer consisting of triphenylene (1,3,5-trinitrobenzene) as the donor (acceptor). The small size of these molecules allows a straightforward for appropriate CT-exciton intersections and demonstrates many of the issues that arise in obtaining the electronic couplings of long-range organic dimers.

Attachment/detachment density plots are presented in Fig. 5-3 for localized and delocalized TDDFT states of triphenylene:1,3,5-trinitrobenzene. We use this attachment/detachment analysis to inspect the electronic character of the first several TDDFT states.

Fig. 5-4 presents the first several singlet TDDFT states and the lowest lying CDFT state of triphenylene:1,3,5-trinitrobenzene. By attachment/detachment analysis, we

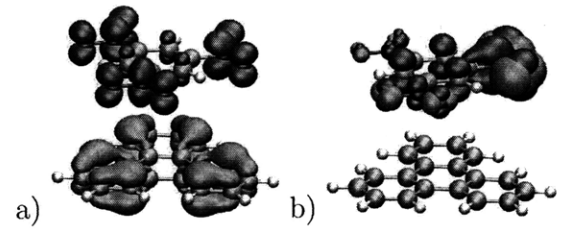

Figure 5-3: Attachment/detachment density plots for triphenylene:1,3,5-trinitrobenzene illustrating a) delocalized CT-like and b) localized exciton-like electron densities. Red (green) regions have excess (deficient) density compared to the ground state.

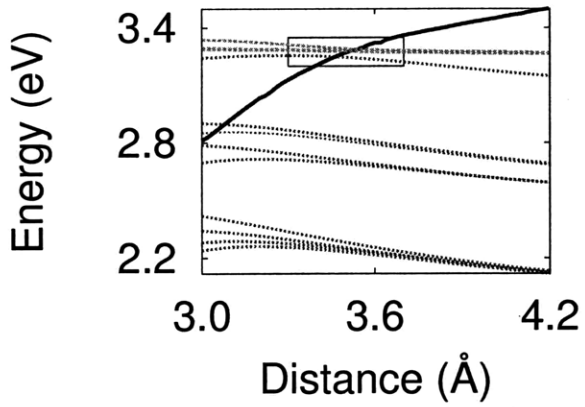

Figure 5-4: Diabatic energy surfaces for TDDFT excitons (dashed green curves), TDDFT CT-like states (dotted red curves) and a CDFT state (solid blue curve) for triphenylene:1,3,5-trinitrobenzene as a function of monomer-monomer separation distance. The inset rectangle encloses crossings of the CT state with three TDDFT excitons and one CT-like TDDFT state.

find that the lowest nine states have CT-like delocalized electronic character as in the left pane of Fig. 5-3, while the higher lying TDDFT states shown in Fig. 5-4 have localized excitonic electronic character (Fig. 5-3b). It is known that for many density functionals such as B3LYP, CT-like states generated by TDDFT have erroneously low energies.[103] Consequently, the lowest nine TDDFT states (red curves) in Fig. 5-4 do not correspond to experimentally observable excitations. Meanwhile, the higher-lying singlet excitations represented by the green curves in Fig. 5-4 are excitons and are expected to correspond to fluoresence absorption spectra.

Excitions are localized on monomers, so they should not change much in energy as the monomer-monomer separation increases. This expection that excitons

will remain nearly constant with respect to separation distance provides a diagnostic for distinguishing excitons from TDDFT CT-like states that compliments attachment/detachment analysis. For this particular dimer, we find that the excition TDDFT states in Fig. 5-4 remain at nearly constant energies with respect to the separation distance, but that the CT-like states erroneously decrease in energy as the monomer-monomer separation distance is increased. Meanwhile, CT states are characterized by charge separation that is delocalized over both monomers. Then, we expect CT state energies to increase as the monomers are separated due to the attractive $\frac{1}{r}$ Columbic potential between the CT state's separated charges. Indeed, we find that the CT state generated by CDFT has a positive slope over the entire range presented in Fig. 5-4.

Since we will treat the TDDFT excitons as diabatic-like states, it is important that they have consistent electronic character as we track along the monomer-monomer separation coordinate. We observe in Fig. 5-4 that all but one of the delocalized CT-like TDDFT states are separated in energy from the excitons. In particular, the highest lying CT-like TDDFT state is energetically near the three lowest lying excitons S_1, S_2 and S_3 at separations less than 3.7 Å. The attachment/detachment densities of S_1, S_2 and S_3 were inspected near 3.5 Å. While S_1 and S_2 were found to have localized densities in this monomer-monome separation range, slight delocalization of the S_3 state's density was observed, indicating that S_3 is not fully adiabatic.

The triphenylene:1,3,5-trinitrobenzene CT state intersects three TDDFT states in the inset rectangle of Fig. 5-4. We computed couplings $\tilde{H}_{ab}$ between the CT state and these three excitons in the region of the crossings. Fig. 5-5 presents the resulting coupling magnitudes. We observe that the couplings are on the order of 1-7 meV and that $\tilde{H}_{CT,S_3} > \tilde{H}_{CT,S_2} > \tilde{H}_{CT,S_1}$. Therefore, if the reorganization energies and driving forces are similar, we expect transitions between S_3 and the CT state to occur more easily than transitions between S_2 or S_1 and the CT state (Eq. 5.1). Another observation is that the couplings tend toward zero for large monomer-monomer separations. This reflects the decreasing orbital overlap between the exciton and CT state. Additionally, we note that although the attachement/detachment density of S_3 shows mild

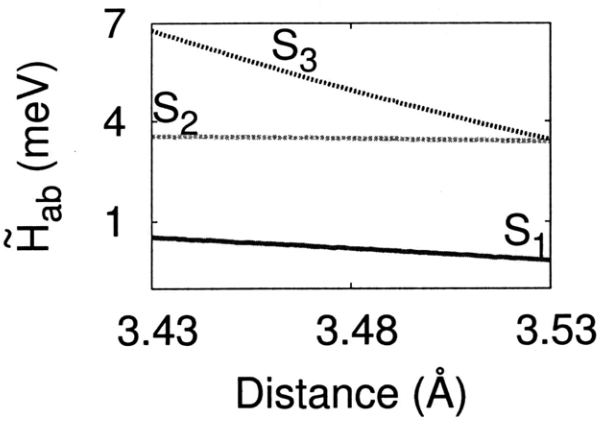

Figure 5-5: Coupling $\tilde{H}_{ab}$ magnitudes between the CT state and S_1, S_2, and S_3 states of triphenylene:1,3,5-trinitrobenzene at the diabatic state crossings where the labels indicated the coupled exciton. We find that the couplings tend toward zero at large separations.

delocalization near 3.5 Å, the magnitudes shown in Fig. 5-5 are consistently small as would be expected for couplings between exciton-like TDDFT states and CT states. It is therefore reasonable to treat S_1, S_2, and S_3 as diabatic states.

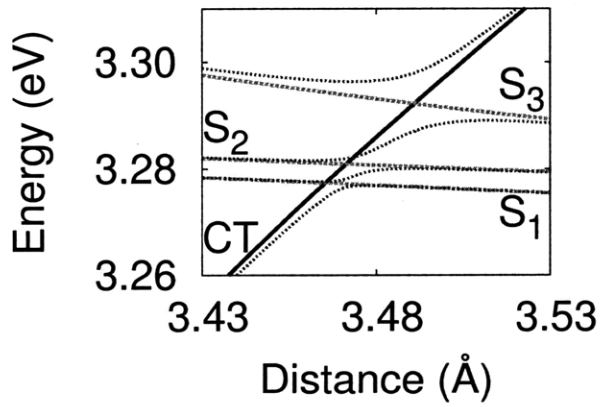

Figure 5-6: Diabatic exciton states (labeled green dashed curves), CT state (labeled solid blue curve), and adiabatic states (dotted red curves) of triphenylene:1,3,5-trinitrobenzene at the intersections of the CT state with S_1, S_2, and S_3.

The four adiabatic states that result from solving Eq. 5.2 for the CT, S_1, S_2, and S_3 diabatic states and couplings are shown in Fig. 5-6. We observe that the adiabatic states avoid each where the diabatic states intersect. Also, the magnitude of the avoided crossing is directly related to the associated coupling magnitude. That

is, the adiabatic states near the CT-S_1 (S_3) crossing most narrowly (strongly) avoid each other because the coupling between these states is small (large). Meanwhile, for regions on the energy surfaces far from avoided crossings, the adiabatic states are almost identical to the diabatic states. Importantly, Fig. 5-6 provides a concrete example of a nonadiabatic transition in an organic heterodimer. For example, suppose that the triphenylene:1,3,5-trinitrobenzene dimer is initially excited to the highest-lying adiabatic surface in Fig. 5-6. Consider how it might undergo relaxation to the lowest adiabatic surface. For monomer-monomer separations less than 3.45 Å, Fig. 5-6 shows that the upper adiabatic surface is electronically similar to the S_3 diabatic surface. Thus, at short enough monomer-monomer separations, the system may easily transition onto the S_3 diabatic surface. Once on the S_3 diabatic surface, if the separation between the dimers increases to distances greater than 3.5 Å, the system can smoothly transition onto the adiabatic surface that connects the S_2 and S_3 diabatic surfaces. Continuing this sequence of steps by alternates between adiabatic and diabatic surfaces and between short and long monomer-monomer separation distances, the system can eventually nonadiabatically transition to the lowest adiabatic surface. These mechanistic details provide an example of the complex transitions that can occur in organic semiconductor materials (Fig. 5-1).

5.3.2 Zn-porphyrin:PTCBI

We have seen that the triphenylene:1,3,5-trinitrobenzene dimer provides an interesting technical demonstration of the constrained coupling method. Let us now study the CT-exciton couplings and resulting adiabatic states of a dimer composed of two organic dyes commonly used in organic semiconductors. PTCBI (3,4,9,10-perylenetetracarboxylic-bis-benzimidazole) is an organic dye often used as as an electron acceptor in OSCs. [145, 171, 172] It absorbs in the 450-800 nm range with absorption maxima near 525 and 700 nm. [173] Meanwhile, Zn-porhyrin is commonly used in dye-sensitized solar cells [174] and in porphrin-fullerene solar cells [175]. Porphyrins have an absorption onset near 450 nm [176] and have an important role in photosynthetic systems. [177, 178]

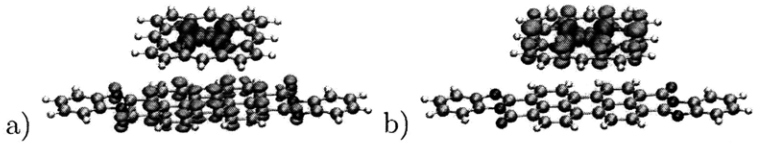

Figure 5-7: Attachment/detachment density plots for Zn-porphyrin:PTCBI illustrating a) delocalized CT-like and b) localized exciton-like TDDFT states. Red (green) regions have excess (deficient) density compared to the ground state.

Attachment/detachment density plots are presented in Fig. 5-7 for localized and delocalized TDDFT states of Zn-porphyrin:PTCBI. We use this attachment/detachment analysis to inspect the electronic character of the first several TDDFT states.

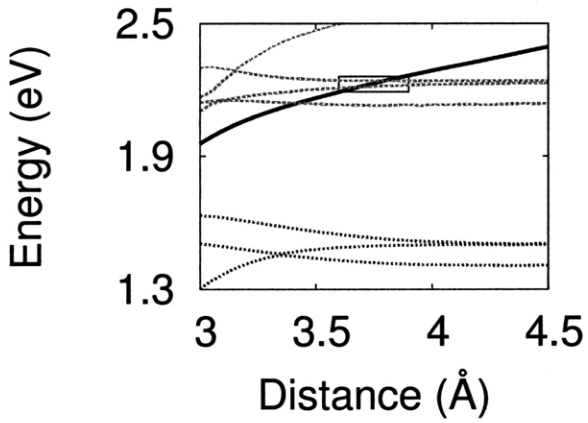

Figure 5-8: Diabatic energy surfaces for TDDFT excitons (dashed green curves), TDDFT CT-like states (dotted red curves) and a CDFT state (solid blue curve) for Zn-porphyrin:PTCBI as a function of monomer-monomer separation distance. The inset rectangle encloses crossings of the CT state with two TDDFT excitons. We see that the localized TDDFT states are energetically separated from the delocalized TDDFT states.

Fig. 5-8 presents the first several singlet TDDFT states and the lowest lying CDFT state of Zn-porphyrin:PTCBI. As for triphenylene:1,3,5-trinitrobenzene (Fig. 5-4), we find that the CDFT state has a positive slope for the entire range inspected. By attachment/detachment analysis, the three TDDFT states below 1.7 eV are identified as CT-like. That is, the lowest singlet exciton states appear above 2.1 eV. Unlike for triphenylene:1,3,5-trinitrobenzene, there is a clear energetic delineation between the CT-like TDDFT states and the excitons, strongly supporting the assumption that these TDDFT states are diabatic-like.

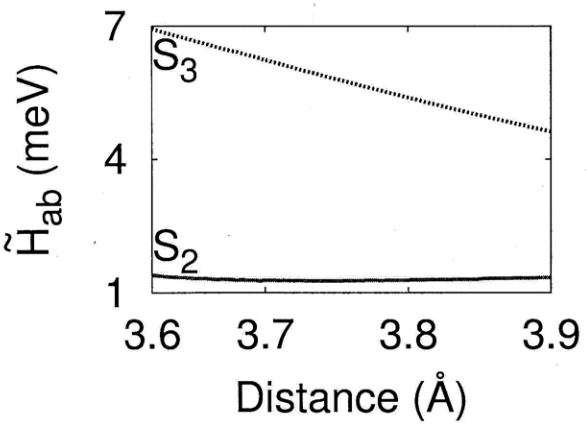

Figure 5-9: Coupling magnitudes near the CT-S_2 and CT-S_3 intersections labeled by the coupled exciton. We find that the CT-S_2 coupling is small over the entire range, and that the CT-S_3 couplings tends toward zero at large separations.

In Fig. 5-8, the CT state intersects three TDDFT states. Fig. 5-9 presents coupling magnitudes $\tilde{H}_{ab}$ for the upper two of these intersections. As in triphenylene:1,3,5-trinitrobenzene (Fig. 5-5), we observe that the couplings are on the order of 0-7 meV and tend toward zero for large monomer-monomer separations. We note that the CT-S_3 coupling is much larger than the CT-S_2 coupling. Thus, by Eq. 5.1, we might expect more facile transitions between S_3 and the CT state than between S_2 and the CT state.

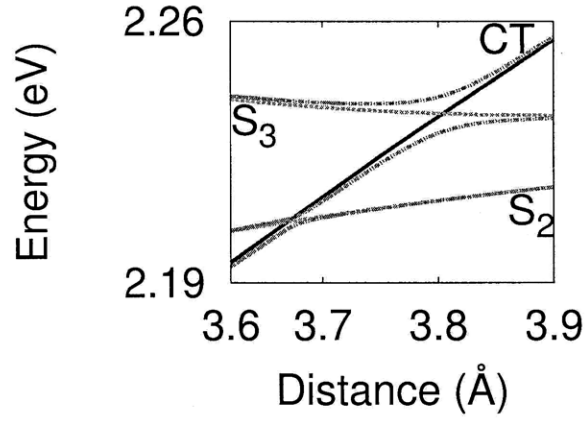

Figure 5-10: Diabatic exciton states (labeled green dashed curves), CT state (labeled solid blue curve), and adiabatic states (dotted red curves) of Zn-porphyrin:PTCBI at the intersections of the CT state with S_2 and S_3.

Fig. 5-10 presents adiabatic and diabatic CT and exciton energy surfaces in the region of the CT-S_2 and CT-S_3 intersections. We observe that the adiabatic states avoid each where the diabatic states intersect. The the avoided crossing magnitudes correspond to their associated coupling magnitude so that the adiabatic states near the CT-S_2 (S_3) crossing narrowly (strongly) avoid each other. Meanwhile, for regions on the energy surfaces far from avoided crossings, the adiabatic states are almost identical to the diabatic states. As for triphenylene:1,3,5-trinitrobenzene, we can propose a sequence of steps by which Zn-porphyrin:PTCBI may smoothly transition from the upper adiabatic state to the lower adiabatic state. Given the roles of PTCBI and Zn-porphyrin as commonly used semiconductor devices, these mechanistic details about their nonadiabatic transitions are of particular interest for guiding the design of advanced solar cells and light-emitting devices.

5.4 Conclusions

We have presented an *ab initio* method for obtaining the electronic couplings between excitons and CT states in organic molecules. The utility of this method has been demonstrated by applying it to the study of the adiabatic and diabatic states and nonadiabatic transitions of two organic dimers. These results provide conceptual details of the mechanisms that allow transitions between CT states and excitons, which is an integral step in the efficient function of organic solar cells and light-emitting devices.

The calculations presented in this work have been conducted in the gas phase. Future efforts to compute these CT-exciton couplings will use condensed phase methods such as QM/MM [122] and implicit solvation models [179] that simulate effects due to bulk polarization and nuclear heterogeneity. These bulk calculations provide reorganization energies and driving forces that may be combined with the electronic couplings to provide estimations of OSC transition rates.

Our coupling methology is amenable to a screening process in which relevant electronic properties are computed for a wide variety of potential OSC molecules.

Those materials that are found to have the most appealing properties can be identified and inspected by experimental means.

Chapter 6

Conclusion

The study of organic semiconductors and the search for superior materials and device architectures remains a challenging problem. In this conclusion, we discuss several ideas for future work.

In Chapter 5, QM/MM was used to model bulk properties of OSC materials. There, the example system was pure Alq_3. Future studies will incorporate two or more materials in the simulation to model the electronic properties of heterojuction interfaces and to account for the effects of sample impurities on trap states. While crystal structures exist for many pure OSC materials, less is known about intermolecular orientations near heterosystem interfaces. This limited information poses a challenge for QM/MM methods. It is reasonable to derive MM force fields for a given pure system from its crystal structure, but it is less clear how to obtain a force field for material blends especially in the region of the interface. The choice of MM force field in these simulations dictates the quality of conformational sampling that can be obtained. Consequently, reliable methods for generating force fields for heterosystems, blends, and systems with impurities will improve the predictive power of QM/MM simulations.

In the near term, progress is being made to obtain reliable estimates for some bulk properties, such as the transport gap, using dielectric continuum models. The advantage of such dielectric continuum models is that bulk molecules are not explicitly included in simulations. This reduces both computational expense and human

intervention required to obtain a result.

Another area for future theoretical studies of OSCs is exciton diffusion. Fig. 1-3 describes the steps by which light is converted into free charge carriers. To generate the CT states, the photogenerated exciton must be at the electron-hole transport interface. If this exciton is generated away from the interface, it must diffuse toward the interface before the CT state may be formed. [9] To model this diffusion process, it is necessary to obtain site energies, electronic couplings, and reorganization energies for the process. The QM/MM approach is expected to be useful for obtaining site and reorganization energies. Effort is underway to efficiently simulate electronic couplings relevant to exciton diffusion.

Figs. 1-3, 3-1, and 5-1 emphasize that OLED and OPV operation involves a complex interplay between free carriers, CT states, excitons, and the ground state. Once all of the state energies, reorganization energies, and coupling elements are known, one goal is to identify the state-to-state pathways that lead to the most efficient energy conversions. Lattice kinetic Monte Carlo approaches show promise in solving this problem. [180]

Bibliography

[1] S. R. Forrest and M. E. Thompson. Introduction: Organic electronics and optoelectronics. *Chem. Rev.*, 107(4):923–925, July 2007.

[2] E. Menard, M. A. Meitl, Y. Sun, J.-U. Park, D. J.-L. Shir, Y.-S. Nam, , S. Jeon, and J. A. Rogers. Micro- and nanopatterning techniques for organic electronic and optoelectronic systems. *Chem. Rev.*, 107(4):1117–1160, July 2007.

[3] CNRS. Renewable energies: The promise of organic solar cells, 2009. Retrieved December 9, 2009, from http://www.sciencedaily.com/releases/2009/04/090409151444.htm.

[4] T. Rousseau, A. Cravino, T. Bura, G. Ulrich, R. Ziessel, and J. Roncali. Multi-donor molecular bulk heterojunction solar cells: improving conversion efficiency by synergistic dye combinations. *J. Mater. Chem.*, 19(16):2298–2300, 2009.

[5] T. Rousseau, A. Cravino, T. Bura, G. Ulrich, R. Ziessel, and J. Roncali. Bodipy derivatives as donor materials for bulk heterojunction solar cells. *Chem. Comm.*, pages 1673–1675, 2009.

[6] Y. Shirota and H. Kageyama. Charge carrier transporting molecular materials and their applications in devices. *Chem. Rev.*, 107(4):953–1010, July 2007.

[7] A. Murphy and J. M. J. Frechét. Organic semiconducting oligomers for use in thin film transistors. *Chem. Rev.*, 107(4):1066–1096, July 2007.

[8] R. R. Lunt, N. C. Giebink, A. A. Belak, J. B. Benziger, and S. R. Forrest. Exciton diffusion lengths of organic semiconductor thin films measured by spectrally resolved photoluminescence quenching. *J. Appl. Phys.*, 105(5):053711, 2009.

[9] V. Coropceanu, J. Cornil, D. A. da Silva Filho, Y. Olivier, R. Silbey, and J. L. Bredás. Charge transport in organic semiconductors. *Chem. Rev.*, 107:926–952, 2007.

[10] A. P. Kulkarni, C. J. Tonzola, A. Babel, and S. A. Jenekhe. Electron transport materials for organic light-emitting diodes. *Chem. Mater.*, 16(23):4556–4573, 2004.

[11] P. W. M. Blom, M. J. M. de Jong, and J. J. M. Vleggaar. Electron and hole transport in poly(p-phenylene vinylene) devices. *Appl. Phys. Lett.*, 68(23):3308–3310, 1996.

[12] C. D. Dimitrakopoulos and D. J. Mascaro. Organic thin-film transistors: a review of recent advances. *IBM Journal of Research and Development*, 45:11–27, 2001.

[13] O. D. Jurchescu, J. Baas, and T. T. M. Palstra. Effect of impurities on the mobility of single crystal pentacene. *Appl. Phys. Lett.*, 84(16):3061–3063, 2004.

[14] S. E. Fritz, S. M. Martin, C. D. Frisbie, M. D. Ward, and M. F. Toney. Structural characterization of a pentacene monolayer on an amorphous sio_2 substrate with grazing incidence x-ray diffraction. *J. Am. Chem. Soc.*, 126:4084–4085, 2004.

[15] C. Goh, R. J. Kline, M. D. McGehee, E. N. Kadnikova, and J. M. J. Fréchet. Molecular-weight-dependent mobilities in regioregular poly(3-hexyl-thiophene) diodes. *Appl. Phys. Lett.*, 86(12):122110, 2005.

[16] T. M. Clarke and J. R. Durrant. Charge photogeneration in organic solar cells. *Chem. Rev.*, 2009. Published ASAP.

[17] J. Kalinowski, M. Cocchi, P. Di Marco, W. Stampor, G. Giro, and V. Fattori. Impact of high electric fields on the charge recombination process in organic light-emitting diodes. *J. Phys. D*, 33(19):2379–2387, 2000.

[18] A. Pivrikas, N. S. Sariciftci, G. Juška, and R. Österbacka. A review of charge transport and recombination in polymer/fullerene organic solar cells. *Progress in Photovoltaics: Research and Applications*, 15(8):677–696, 2007.

[19] H. Imahori, K. Tamaki, D. M. Guldi, C. Luo, M. Fujitsuka, O. Ito, Y. Sakata, and Shunichi Fukuzumi. Modulating charge separation and charge recombination dynamics in porphyrin-fullerene linked dyads and triads: Marcus-normal versus inverted region. *J. Am. Chem. Soc.*, 123(11):2607–2617, 2001.

[20] T. Ameri, G. Dennler, C. Lungenschmied, and C. J. Brabec. Organic tandem solar cells: A review. *Energy and Environmental Science*, 2(4):347–363, 2009.

[21] R. Häusermann, E. Knapp, M. Moos, N. A. Reinke, T. Flatz, and B. Ruhstaller. Coupled optoelectronic simulation of organic bulk-heterojunction solar cells: Parameter extraction and sensitivity analysis. *J. Appl. Phys.*, 106(10):104507, 2009.

[22] I. A. Howard, F. Laquai, P. E. Keivanidis, R. H. Friend, and N. C. Greenham. Perylene tetracarboxydiimide as an electron acceptor in organic solar cells: A study of charge generation and recombination. *J. Phys. Chem. C*, 113(50):21225–21232, 2009.

[23] I. Hwang, C. R. McNeill, and N. C. Greenham. Drift-diffusion modeling of photocurrent transients in bulk heterojunction solar cells. *J. Appl. Phys.*, 106(9):094506, 2009.

[24] J.J. Benson-Smith, L. Goris, K. Vandewal, K. Haenen, J.V. Manca, D. Vanderzande, D.D.C. Bradley, and J. Nelson. Formation of a ground-state charge-transfer complex in polyfluorene//[6,6]-phenyl-c61 butyric acid methyl ester (pcbm) blend films and its role in the function of polymer/pcbm solar cells. *Adv. Funct. Mater.*, 17:451–457, 2007.

[25] A. C. Morteani, R. H. Friend, and C. Silva. Endothermic exciplex-exciton energy-transfer in a blue-emitting polymeric heterojunction system. *Chem. Phys. Lett.*, 391(1-3):81 – 84, 2004.

[26] K. Tvingstedt, K. Vandewal, A. Gadisa, F. Zhang, J. Manca, and O. Ingans. Electroluminescence from charge transfer states in polymer solar cells. *J. Am. Chem. Soc.*, 131:11819–11824, 2009.

[27] L. Goris, A. Poruba, L. Hod'ákova, M. Vaněček, K. Haenen, M. Nesládek, P. Wagner, D. Vanderzande, L. De Schepper, and J. V. Manca. Observation of the subgap optical absorption in polymer-fullerene blend solar cells. *Appl. Phys. Lett.*, 88(5):052113, 2006.

[28] T. Drori, C.-X. Sheng, A. Ndobe, S. Singh, J. Holt, and Z. V. Vardeny. Below-gap excitation of π-conjugated polymer-fullerene blends: Implications for bulk organic heterojunction solar cells. *Phys. Rev. Lett.*, 101(3):037401, 2008.

[29] H. Ohkita, S. Cook, Y. Astuti, W. Duffy, M. Heeney, S. Tierney, I. McCulloch, D. D. C. Bradley, and James R. Durrant. Radical ion pair mediated triplet formation in polymer-fullerene blend films. *Chem. Comm.*, pages 3939–3941, 2006.

[30] A. A. Bakulin, D. S. Martyanov, D. Yu. Paraschuk, M. S. Pshenichnikov, and P. H. M. van Loosdrecht. Ultrafast charge photogeneration dynamics in ground-state charge-transfer complexes based on conjugated polymers. *J. Phys. Chem. B*, pages 13730–13737, 2008.

[31] V. Gulbinas, D. Hertel, A. Yartsev, and V. Sundström. Charge carrier photogeneration and recombination in ladder-type poly(para-phenylene): Interplay between impurities and external electric field. *Phys. Rev. B*, 76(23):235203, 2007.

[32] H. Ohkita, S. Cook, Y. Astuti, W. Duffy, S. Tierney, W. Zhang, M. Heeney, I. McCulloch, J. Nelson, D. D. C. Bradley, and J. R. Durrant. Charge carrier formation in polythiophene/fullerene blend films studied by transient absorption spectroscopy. *J. Am. Chem. Soc.*, 130:3030–3042, 2008.

[33] M. M. Mandoc, F. B. Kooistra, J. C. Hummelen, B. de Boer, and P. W. M. Blom. Effect of traps on the performance of bulk heterojunction organic solar cells. *Appl. Phys. Lett.*, 91(26):263505, 2007.

[34] P. Hohenberg and W. Kohn. Inhomogeneous electron gas. *Phys. Rev.*, 136(3B):B864–B871, 1964.

[35] R. G. Parr and W. Yang. *Density-Functional Theory of Atoms and Molecules.* Oxford Science Press, 1989.

[36] W. Kohn and L. J. Sham. Self-consistent equations including exchange and correlation effects. *Phys. Rev.*, 140(4A):A1133–A1138, 1965.

[37] A. D. Becke. Density-functional exchange-energy approximation with correct asymptotic behavior. *Phys. Rev. A*, 38(6):3098–3100, Sep 1988.

[38] A. Dreuw and M. Head-Gordon. Single-reference ab initio methods for the calculation of excited states of large molecules. *Chem. Rev.*, 105:4009–4037, 2005.

[39] Q. Wu and T. Van Voorhis. Direct optimization method to study constrained systems within density-functional theory. *Phys. Rev. A*, 72:024502, 2005.

[40] I. Rudra, Q. Wu, and T. Van Voorhis. Accurate magnetic exchange couplings in transition-metal complexes from constrained density-functional theory. *J. Chem. Phys.*, 124:24103, 2006.

[41] Q. Wu and T. Van Voorhis. Constrained density functional theory and its application in long-range electron transfer. *J. Chem. Theory Comput.*, 2:765–774, 2006.

[42] Q. Wu and T. Van Voorhis. Direct calculation of electron transfer parameters through constrained density functional theory. *J. Phys. Chem. A*, 110:9212–9218, 2006.

[43] Q. Wu and T. Van Voorhis. Extracting electron transfer coupling elements from constrained density functional theory. *J. Chem. Phys.*, 125:164105, 2006.

[44] R. H. Friend, R. W. Gymer, A. B. Holmes, J. H. Burroughes, R. N. Marks, C. Taliani, D. D. C. Bradley, D. A. Dos Santos, J. L. Bredas, M. Logdlund, and W. R. Salaneck. Electroluminescence in conjugated polymers. *Nature*, 397:121–128, 1999.

[45] G. Horowitz. Organic field-effect transistors. *Adv. Mat.*, 10:365–377, 1998.

[46] A. J. Nozik. Photoelectrochemistry: Applications to solar energy conversion. *Annual Review of Physical Chemistry*, 29:189–222, 1978.

[47] U. Mitschke and P. Bauerle. The electroluminescence of organic materials. *J. Mat. Chem.*, 10:1471–1507, 2000.

[48] P. Judenstein and C. Sanchez. Hybrid organic-inorganic materials: a land of multidisciplinarity. *J. Mat. Chem.*, 6:511–525, 1996.

[49] J.-L. Bredás, D. Beljonne, V. Coropceanu, and J. Cornil. Charge-transfer and energy-transfer processes in π-conjugated oligimers and polymers: a molecular picture. *Chem. Rev.*, 104:4971–5003, 2004.

[50] J. R. Sheats, H. Antoniadis, M. Hueschen, W. Leonard, J. Miller, R. Moon, D. Roitman, and A. Stocking. Organic electroluminescent devices. *Science*, 273:884–888, 1996.

[51] S. R. Forrest. The path to ubiquitous and low-cost organic electronic appliances on plastic. *Nature*, 428:911–918, 2004.

[52] B. Geffroy, P. le Roy, and C. Prat. Organic light-emitting diode (oled) technology: materials, devices and display technologies. *Polymer International*, 55:572–582, 2006.

[53] Z. Shen, P. E. Burrows, V. Bulović, S. R. Forrest, and M. E. Thompson. Three-color, tunable, organic light-emitting devices. *Science*, 276:2009–2011, 1997.

[54] W. Helfrich and W. G. Schneider. Recombination radiation in anthracene crystals. *Phys. Rev. Lett.*, 14:229–231, 1965.

[55] H. Yersin. Triplet emitters for oled applications. mechanisms of exciton trapping and control of emission properties. *Top. Curr. Chem.*, 241:1–26, 2004.

[56] M. Segal, M. A. Baldo, R. J. Holmes, S. R. Forrest, and Z. G. Soos. Excitonic singlet-triplet ratios in molecular and polymeric organic materials. *Phys. Rev. B*, 68(7):075211, 2003.

[57] L. C. Lin, H. F. Meng, J. T. Shy, S. F. Horng, L. S. Yu, C. H. Chen, H. H. Liaw, C. C. Huang, K. Y. Peng, and S. A. Chen. Triplet-to-singlet exciton formation in poly(*p*-phenylene-vinylene) light-emitting diodes. *Phys. Rev. Lett.*, 90(3):036601, 2003.

[58] Y. Cao, I. D. Parker, G. Yu, C. Zhang, and A. J. Heeger. Improved quantum efficiency for electroluminescence in semiconducting polymers. *Nature*, 397:414–417, 1998.

[59] P. K. H. Ho, J.-S. Kim, J. H. Burroughes, H. Becker, S. F. Y. Li, T. M. Brown, F. Cacialli, and R. H. Friend. Molecular-scale interface engineering for polymer light-emitting diodes. *Nature*, 404:481–484, 2000.

[60] J. S. Wilson, A. S. Dhoot, A. J. A. B. Seeley, M. S. Khan, A. Köhl, and R. H. Friend. Spin-dependent exciton formation in pi-conjugated compounds. *Nature*, 413:828–831, 2001.

[61] M. Wohlgenannt, K. Tandon, S. Mazumdar, S. Ramasesha, and Z. V. Vardeny. Formation cross-sections of singlet and triplet excitons in π-conjugated polymers. *Nature*, 409:494–497, 2001.

[62] M. Wohlgenannt, X. M. Jiang, Z. V. Vardeny, and R. A. J. Janssen. Conjugation-length dependence of spin-dependent exciton formation rates in π-conjugated oligomers and polymers. *Phys. Rev. Lett.*, 88(19):197401, 2002.

[63] M. Wohlgenannt, C. Yang, and Z. V. Vardeny. Spin-dependent delayed luminescence from nongeminate pairs of polarons in π-conjugated polymers. *Phys. Rev. B*, 66(24):241201, 2002.

[64] A. S. Dhoot, D. S. Ginger, D. Beljonne, Z. Shuai, and N. C. Greenham. Triplet formation and decay in conjugated polymer devices. *Chem. Phys. Lett.*, 360:195–201, 2002.

[65] Z. Shuai, D. Beljonne, R. J. Silbey, and J. L. Bredás. Singlet and triplet exciton formation rates in conjugated polymer light-emitting diodes. *Phys. Rev. Lett.*, 84:131–134, 2000.

[66] M. Wohlgenannt. Polarons in π-conjugated semiconductors: absorption spectroscopy and spin-dependent recombination. *Phys. Stat. Sol. A*, 201:1188–1204, 2004.

[67] M. Wohlgenannt and Z. V. Vardeny. Spin-dependent exciton formation rates in π-conjugated materials. *Journal of Physics: Condensed Matter*, 15(3):R83–R107, 2003.

[68] W. Barford. Theory of singlet exciton yield in light-emitting polymers. *Phys. Rev. B*, 70:205204, 2004.

[69] M. N. Kobrak and E. R. Bittner. Quantum molecular dynamics study of polaron recombination in conjugated polymers. *Phys. Rev. B*, 62:11473, 2000.

[70] J. Staudigel, M. Stößel, F. Steuber, and J. Simmerer. A quantitative numerical model of multilayer vapor-deposited organic light emitting diodes. *J. Appl. Phys.*, 86:3895–3910, 1999.

[71] A. L. Burin and M. A. Ratner. Spin effects on the luminescence yield of organic light emitting diodes. *J. Chem. Phys.*, 109:6092–6102, 1998.

[72] S. Karabunarliev and E. R. Bittner. Dissipative dynamics of spin-dependent electron-hole capture in conjugated polymers. *J. Chem. Phys.*, 119:3988–3995, 2003.

[73] T.-M. Hong and H.-F. Meng. Spin-dependent recombination and electroluminescence quantum yield in conjugated polymers. *Phys. Rev. B*, 63(7):075206, 2001.

[74] A. Ye, Z. Shuai, and J. L. Brédas. Coupled-cluster approach for studying the singlet and triplet exciton formation rates in conjugated polymer led's. *Phys. Rev. B*, 65(4):045208, 2002.

[75] K.j Tandon, S. Ramasesha, and S. Mazumdar. Electron correlation effects in electron-hole recombination in organic light-emitting diodes. *Phys. Rev. B*, 67(4):045109, 2003.

[76] A. Köhle, J. S. Wilson, R. H. Friend, M. K. Al-Suti, M. S. Khan, A. Gerhard, and H. Bässler. The singlettriplet energy gap in organic and pt-containing phenylene ethynylene polymers and monomers. *J. Chem. Phys.*, 116:9457–9463, 2002.

[77] C. Rothe, K. Brunner, I. Bach, S. Heun, and A. P. Monkman. Effects of triplet exciton confinement induced by reduced conjugation length in polyspirobifluorene copolymers. *J. Chem. Phys.*, 122:084706, 2005.

[78] M. Reufer, M. J. Walter, A. B. Hummel Lagoudakis, P. G., J. S. Kolb, H. G. Roskos, U. Scherf, and J. M. Lupton. Spin-conserving carrier recombination in conjugated polymers. *Nat. Mat.*, 4:340–346, 2005.

[79] M. Segal, M. Singh, K. Rivoire, S. Difley, T. Van Voorhis, and M. A. Baldo. Extrafluorescent electroluminescence in organic light-emitting devices. *Nat. Mater.*, 6:374–378, 2007.

[80] T. Ziegler, A. Rauk, and E. J. Baerends. On the calculation of multiplet energies by the hartree-fock-slater method. *Theoret. Chim. Acta*, 43:261–271, 1977.

[81] E. J. Bylaska, W. A. de Jong, K. Kowalski, T. P. Straatsma, M. Valievand D. Wang, E. Apr, T. L. Windusand S. Hirata, M. T. Hackler, Y. Zhao, P.-D. Fan, R. J. Harrison, M. Dupuis, D. M. A. Smith, J. Nieplocha, V. Tipparaju, M. Krishnan, A. A. Auer, M. Nooijen, E. Brown, G. Cisnerosand, G. I. Fann, H. Frchtl, J. Garza, K. Hirao, R. Kendall, J. A. Nichols, K. Tsemekhman, K. Wolinski, J. Anchell, D. Bernholdt, P. Borowski, T. Clark, D. Clerc, H. Dachsel, M. Deegan, K. Dyall, D, Elwood, E. Glendening, M. Gutowski, A. Hess, J. Jaffe, B. Johnson, J. Ju, R. Kobayashi, R. Kutteh, Z. Lin, R. Littlefield, X. Longand B. Meng, T. Nakajima, S. Ni, L. Pollack, M. Rosing, G. Sandrone, M. Stave, H. Taylorand G. Thomas, J. van Lenthe, A. Wong, and Z. Zhang. Nwchem, a computational chemistry package for parallel computers, version 4.6, pacific northwest national laboratory, richland, washington 99352-0999, usa, 2004.

[82] J. Kong, C. A. White, A. I. Krylov, C. D. Sherrill, R. D. Adamson, T. R. Furlani, M. S. Lee, A. M. Lee, S. R. Gwaltney, T. R. Adams, H. Daschel, W. Zhang, P. P. Korambath, C. Ochsenfeld, A. T. B. Gilbert, G. S. Kedziora, D. R. Maurice, N. Nair, Y. Shao, N. A. Besley, P. E. Maslen, J. P. Dombroski, J. Baker, E. F. C. Byrd, T. Van Voorhis, M. Oumi, S. Hirata, C.-P. Hsu, N. Ishikawa, J. Florian,

A. Warshel, B. G. Hohnson, P. M. W. Gill, M. Head-Gordon, , and J. A. Pople. Q-chem 2.0: a high-performance ab initio electronic structure program package. *J. Comp. Chem.*, 21:1532–1548, 2000.

[83] A. D. Becke. A multicenter numerical integration scheme for polyatomic molecules. *J. Chem. Phys.*, 88:2547, 1988.

[84] M. Cölle, R. E. Dinnebier, and W. Brütting. The structure of the blue luminescent δ-phase of tris(8-hydroxyquinoline)aluminium(iii) (alq3). *Chem. Comm.*, 23:2908–2909, 2002.

[85] M. Braun, J. Gmeiner, M. Tzolov, M. Coelle, F. D. Meyer, W. Milius, H. Hillebrecht, O. Wendland, J. U. von Schütz, and W. Brütting. A new crystalline phase of the electroluminescent material tris(8-hydroxyquinoline) aluminum exhibiting blueshifted fluorescence. *J. Chem. Phys.*, 114:9625–9632, 2001.

[86] W.-L. Jia, T. McCormick, Q. D. Liu, H. Fukutani, M. Motala, R.-Y. Wang, Y. Tao, and S. Wang. Diarylamino functionalized pyrene derivatives for use in blue oleds and complex formation. *J. Mater. Chem.*, 14:3344–3350, 2004.

[87] X. Junfeng, J. Qiao, L. Wang, J. Xie, and Y. Qiu. An azomethin-zinc complex for organic electroluminescence: Crystal structure, thermal stability and optoelectronic properties. *Inorg. Chim. Acta*, 358:4451–4458, 2005.

[88] M. A. Harvey, S. Baggio, A. Ibañez, and R. Baggio. Three zinc(ii) complexes presenting a znn_6 chromophore and with peroxodisulfate as the counter-ion. *Acta. Cryst.*, C60(8):m375–m381, Jul 2004.

[89] M. Brinkmann, G. Gadret, M. Muccini, C. Taliani, N. Masciocchi, and A. Sironi. Correlation between molecular packing and optical properties in different crystalline polymorphs and amorphous thin films of mer-tris(8-hydroxyquinoline)aluminum(iii). *J. Am. Chem. Soc.*, 122:5147–5157, 2000.

[90] M. Cölle and C. Gärditz. Delayed fluorescence and phosphorescence of tris-(8-hydroxyquinoline)aluminum (alq3) and their temperature dependence. *J. Lumin.*, 110:200–206, 2004.

[91] M. Cölle and C. Gärditz. Phosphorescence of aluminum tris(quinoline-8-olate). *Appl. Phys. Lett.*, 84:3160–3162, 2004.

[92] P. W. Anderson. New approach to the theory of superexchange interactions. *Phys. Rev.*, 115(1):2, 1959.

[93] J. B. Goodenough. Direct cation- -cation interactions in several oxides. *Phys. Rev.*, 117(6):1442–1451, Mar 1960.

[94] J. Kanamori. Superexchange interaction and symmetry properties of electron orbitals. *J. Phys. Chem. Solids*, 10:87, 1958.

[95] J. Rissler and H. Bässler. Excited states of ladder-type poly-p-phenylene oligomers. *Phys. Rev. B*, 64:45122, 2001.

[96] T. Gustavsson, G. Baldacchino, J.-C. Mialocq, and S. Pommeret. A femtosecond fluorescence up-conversion study of the dynamic stokes shift of the dcm dye molecule in polar and non-polar solvents. *Chem. Phys. Letters*, 236:587–594, 1995.

[97] S. Tsuzuki and H. P. Lüthi. Interaction energies of van der waals and hydrogen bonded systems calculated using density functional theory: Assessing the pw91 model. *J. Chem. Phys.*, 114:3949–3957, 2001.

[98] S. Tokito, T. Iijima, Y. Suzuri, H. Kita, T. Tsuzuki, and F. Sato. Confinement of triplet energy on phosphorescent molecules for highly-efficient organic blue-light-emitting devices. *Appl. Phys. Lett.*, 83:569–571, 2003.

[99] Y. Hamada, H. Kanno, H. Tsujioka, T.and Takahashi, and T. Usuki. Red organic light-emitting diodes using an emitting assist dopant. *Appl. Phys. Lett.*, 75:1682–1684, 1999.

[100] Y. T. Tao, C. W. Ko, and E. Balasubramaniam. Energy transfer vs. carrier trapping: emission mechanism in dye-doped organic light emitting diodes. *Thin Sol. Films*, 417:61–66, 2002.

[101] M. A. Baldo, D. F. O'Brien, Y. You, A. Shoustikov, S. Sibley, M. E. Thompson, and S. R. Forrest. Highly efficient phosphorescent emission from organic electroluminescent devices. *Nature*, 395:151–154, 1998.

[102] A. Kadashchuk, A. Vakhnin, I. Blonski, D. Beljonne, Z. Shuai, J. L. Bredás, V. I. Arkhipov, P. Heremans, E. V. Emelianova, and H. Bässler. Singlet-triplet splitting of geminate electron-hole pairs in conjugated polymers. *Physical Review Letters*, 93(6):066803, 2004.

[103] A. Dreuw and M. Head-Gordon. Failure of time-dependent density functional theory for long-range charge-transfer excited states: The zincbacteriochlorin-bacteriochlorin and bacteriochlorophyllspheroidene complexes. *J. Am. Chem. Soc.*, 126:4007–4016, 2004.

[104] A. Klamt and G. Schüürmann. Cosmo: a new approach to dielectric screening in solvents with explicit expressions for the screening energy and its gradient. *J. Chem. Soc. Perkin Trans. 2*, 1993:799–805, 1993.

[105] Z. Shuai and J. L. Brédas. Static and dynamic third-harmonic generation in long polyacetylene and polyparaphenylene vinylene chains. *Phys. Rev. B*, 44(11):5962–5965, 1991.

[106] J. Cornil, D. A. dos Santos, X. Crispin, R. Silbey, and J. L. Brédas. Influence of interchain interactions on the absorption and luminescence of conjugated

oligomers and polymers: A quantum-chemical characterization. *J. Am. Chem. Soc.*, 120:1289–1299, 1998.

[107] E. K. U. Gross, J. F. Dobson, and M. Petersilka. null. *Top. Curr. Chem.*, 181:81, 1996.

[108] P. Peumans, A. Yakimov, and S. R. Forrest. Small molecular weight organic thin-film photodetectors and solar cells. *J. Appl. Phys.*, 93:3693–3723, 2003.

[109] S. F. Nelson, Y. Y. Lin, D. J. Gundlach, and T.N. Jackson. Temperature-independent transport in high-mobility pentacene transistors. *App. Phys. Lett.*, 72:1854–1856, 1998.

[110] S. Difley, D. Beljonne, and T. Van Voorhis. On the singlet-triplet splitting of geminate electron-hole pairs in organic semiconductors. *J. Am. Chem. Soc*, 130:3420–3427, 2008.

[111] M. Cölle and C. Gärditz. Phosphorescence of aluminum tris(quinoline-8-olate). *Appl. Phys. Lett.*, 84(16):3160–3162, 2004.

[112] P. E. Burrows, L. S. Sapochak, D. M. McCarty, S. R. Forrest, and M. E. Thompson. Metal-ion dependent luminescence effects in metal tris-quinolate organic heterojunction light-emitting devices. *Appl. Phys. Lett.*, 64(20):2718–2720, 1994.

[113] M. Pope and C. E. Swenberg. *Electronic Processes in Organic Crystals and Polymers.* Oxford University Press, New York, 1999.

[114] S. R. Forrest. The path to ubiquitous and low-cost organic electronic appliances on plastic. *Nature*, 428:911–918, 2004.

[115] W. Q. Deng and W. A. Goddard. Predictions of hole mobilities in oligoacene organic semiconductors from quantum mechanical calculations. *J. Phys. Chem. B*, 108:8614–8621, 2004.

[116] R. A. Marcus. Theory of oxidation-reduction reactions involving electron transfer. *J. Chem. Phys.*, 24:966–978, 1956.

[117] J. L. Bredás, J. P. Calbert, D. A. da Silva, and J. Cornil. Organic semiconductors: a theoretical characterization of the basic parameters governing charge transport. *Proc. Natl. Acad. Sci. U. S. A.*, 99:5804–5809, 2002.

[118] S. Kilina, E. R. Batista, P. Yang, S. Tretiak, A. Saxena, R. L. Martin, and D. L. Smith. Electronic structure of self-assembled amorphous polyfluorenes. *ACS Nano*, 2:1381–1388, 2008.

[119] G. D. Scholes and R. D. Harcourt. Configuration interaction and the theory of electronic factors in energy transfer and molecular exciton interactions. *J. Chem. Phys.*, 104:5054–5061, 1996.

[120] J. J. Kwiatkowski, J. Nelson, H. Li, J. L. Bredás, W. Wenzel, and C. Lennartz. Simulating charge transport in tris(8-hydroxyquinoline) aluminium (alq3). *Phys. Chem. Chem. Phys.*, 10:1852–1858, 2008.

[121] P. K. Nayak and N. Periasamy. Calculation of electron affinity, ionization potential, transport gap, optical band gap and exciton binding energy of organic solids using solvation model and dft. *Org. Electron.*, page In Press, 2009.

[122] J. Aaqvist and A. Warshel. Simulation of enzyme reactions using valence bond force fields and other hybrid quantum/classical approaches. *Chem. Rev.*, 93:2523–2544, 1993.

[123] J. E. Norton and J. L. Bredás. Polarization energies in oligoacene semiconductor crystals. *J. Am. Chem. Soc.*, 130:12377–12384, 2008.

[124] D. Z. Garbuzov, V. Bulovic, P. E. Burrows, and S. R. Forrest. Photoluminescence efficiency and absorption of aluminum-tris-quinolate (alq3) thin films. *Chem. Phys. Lett.*, 249:433–437, 1996.

[125] A. Curioni and W. Andreoni. Computer simulations for organic light-emitting diodes. *IBM J. Res. Dev.*, 45:101–113, 2001.

[126] Q. Wu and T. Van Voorhis. Direct calculation of electron transfer parameters through constrained density functional theory. *J. Phys. Chem. A*, 110:9212–9218, 2006.

[127] T. Van Voorhis, T. Kowalczyk, B. Kaduk, L. P. Wang, C. L. Cheng, and Q. Wu. The diabatic picture of electron transfer, reaction barriers, and molecular dynamics. *Ann. Rev. Phys. Chem.*, 61:In press, 2010.

[128] T. Pacher, L. S. Cederbaum, and H. Köppel. Adiabatic and quasidiabatic states in a gauge theoretical framework. *Adv. Chem. Phys.*, 84:293–391, 1993.

[129] Q. Wu and T. Van Voorhis. Direct optimization method to study constrained systems within density-functional theory. *Phys. Rev. A*, 72:024502, 2005.

[130] H. Oberhofer and J. Blumberger. Charge constrained density functional molecular dynamics for simulation of condensed phase electron transfer reactions. *J. Chem. Phys.*, 131:064101, 2009.

[131] Q. Wu and Q. Van Voorhis. Extracting electron transfer coupling elements from constrained density functional theory. *J. Chem. Phys.*, 125:164105, 2006.

[132] G. Lamoureux and B. Roux. Modeling induced polarization with classical Drude oscillators: Theory and molecular dynamics simulation algorithm. *J. Chem. Phys.*, 119(6):3025–3039, 2003.

[133] I. G. Hill, A. Kahn, Z. G. Soos, and R. A. Pascal, Jr. Charge-separation energy in films of [pi]-conjugated organic molecules. *Chem. Phys. Lett.*, 327:181–188, 2000.

[134] S. Krause, M. B. Casu, A. Scholl, and E. Umbach. Determination of transport levels of organic semiconductors by ups and ips. *New J. Phys.*, 10:085001, 2008.

[135] M. Brinkmann, G. Gadret, M. Muccini, C. Taliani, N. Masciocchi, and A. Sironi. Correlation between molecular packing and optical properties in different crystalline polymorphs and amorphous thin films of mer-tris(8-hydroxyquinoline)aluminum(iii). *J. Am. Chem. Soc.*, 122(21):5147–5157, 2000.

[136] B. C. Lin, C. P. Cheng, Z. Q. You, and C. P. Hsu. Charge transport properties of tris(8-hydroxyquinolinato)aluminum(iii): why it is an electron transporter. *J. Amer. Chem. Soc.*, 127:66–67, 2004.

[137] B. Hess, C. Kutzner, D. van der Spoel, and E. Lindahl. Gromacs 4: Algorithms for highly efficient, load-balanced, and scalable molecular simulation. *J. Chem. Theory Comput.*, 4(3):435–447, 2008.

[138] B. R. Brooks, R. E. Bruccoleri, B. D. Olafson, D. J. States, S. Swaminathan, and M. Karplus. Charmm - a program for macromolecular energy, minimization, and dynamics calculations. *J. Comput. Chem.*, 4(2):187–217, 1983.

[139] H. L. Woodcock III, M. Hodošček, A. T. B. Gilbert, P. M. W. Gill, H. F. Shaefer III, and B. R. Brooks. Interfacing q-chem and charmm to perform qm/mm reaction path calculations. *J. Comp. Chem.*, 28:1485–1502, 2007.

[140] P. I. Djurovich, E. I. Mayo, S. R. Forrest, and M. E. Thompson. Measurement of the lowest unoccupied molecular orbital energies of molecular organic semiconductors. *Org. Electron.*, 10:515–520, 2009.

[141] A. Schmidt, M. L. Anderson, and N. R. Armstrong. Electronic states of vapor deposited electron and hole transport agents and luminescent materials for light-emitting diodes. *J. Appl. Phys.*, 78:5619–5625, 1995.

[142] R. L. Martin, Joel D. Kress, I. H. Campbell, and D. L. Smith. Molecular and solid-state properties of tris-(8-hydroxyquinolate)-aluminum. *Phys. Rev. B*, 61(23):15804–15811, Jun 2000.

[143] I. Tanaka and S Tokito. Phosphorescent-sensitized triplet-triplet annihilation in tris 8-hydroxyquinoline aluminum. *J. Appl. Phys.*, 97:113532, 2005.

[144] H. D. Burrows, M. Fernandes, J. S. de Melo, A. P. Monkman, and S. Navaratnam. Characterization of the triplet state of tris(8-hydroxyquinoline)aluminium(iii) in benzene solution. *J. Am. Chem. Soc.*, 125:15310–15311, 2003.

[145] C. W. Tang. Two-layer organic photovoltaic cell. *Appl. Phys. Lett.*, 48:183, 1986.

[146] G Li, V Shrotriya, JS Huang, Y Yao, T Moriarty, K Emery, and Y Yang. High-efficiency solution processable polymer photovoltaic cells by self-organization of polymer blends. *Nat. Mater.*, 4:864–868, 2005.

[147] J. Xue, B. P. Rand, S. Uchida, and S. R. Forrest. A hybrid planar-mixed molecular heterojunction photovoltaic cell. *Adv. Mater.*, 17:66–70, 2005.

[148] S. H. Park, A. Roy, S. Beaupr, S. Cho, N. Coates, J. S. Moon, D. Moses, M. Leclerc, K. Lee, and A. J. Heeger. Bulk heterojunction solar cells with internal quantum efficiency approaching 100%. *Nat. Photonics*, 3:297–302, 2009.

[149] J. Y. Kim, K. Lee, N. E. Coates, D. Moses, T. Nguyen, M. Dante, and A. J. Heeger. Efficient tandem polymer solar cells fabricated by all-solution processing. *Science*, 317:222–225, 2007.

[150] L. J. A. Koster, V. D. Mihailetchi, and P. W. M. Blom. Ultimate efficiency of polymer/fullerene bulk heterojunction solar cells. *Appl. Phys. Lett.*, 88:093511, 2006.

[151] B. P. Rand, D. P. Burk, and S. R. Forrest. Offset energies at organic semiconductor heterojunctions and their influence on the open-circuit voltage of thin-film solar cells. *Phys. Rev. B*, 75:115327, 2007.

[152] M. Riede, T. Mueller, W. Tress, R. Schueppel, and K. Leo. Small-molecule solar cells - status and perspectives. *Nanotechnology*, 19:424001, 2008.

[153] W. Helfirch and W. G. Scheinder. Recombination radiation in anthracene crystals. *Phys. Rev. Lett.*, 14:229–231, 1965.

[154] M. Pope, H. P. Kallmann, and P. Magnante. Electroluminescence in organic crystals. *J. Chem. Phys.*, 38:2042, 1963.

[155] S. A. van Slyke and C. W. Tang. Organic electroluminescent diodes. *Appl. Phys. Lett.*, 51:913–915, 1987.

[156] J. H. Burroughes, D. C. C. Bradley, A. R. Brown, R. N. Marks, K. Mackay, R. H. Friend, P. L. Burns, and A. B. Holmes. Light-emitting-diodes based on conjugated polymers. *Nature*, 347:539–541, 1990.

[157] M. A. Baldo, M. E. Thompson, and S. R. Forrest. High-efficiency fluorescent organic light-emitting devices using a phosphorescent sensitizer. *Nature*, 403:750–753, 2000.

[158] P. Heremans, D. Cheyns, and B. Rand. Strategies for increasing the efficiency of hereojuction organic solar cells: material selection and device achitecture. *Acc. Chem. Res.*, 42:1740–1747, 2009.

[159] J. Nelson, J. J. Kwiatkowski, J. Kirkpatrick, and J. M. Frost. Modeling charge transport in organic photovoltaic materials. *Acc. Chem. Res.*, 42:1768–1778, 2009.

[160] X.-Y. Zhu, Q. Yang, and M. Muntwiler. Charge-transfer excitons at organic semiconductor surfaces and interfaces. *Acc. Chem. Res.*, 42:1779–1787, 2009.

[161] R. J. Cave and M. D. Newton. Generalization of the mulliken-hush threatment for the calculation of electron transfer matrix elements. *Chem. Phys. Lett.*, 249:15–19, 1996.

[162] T. Kawatsu, V. Coropceanu, A. Ye, and J. L. Bredás. Quantum-chemical approach to electronic coupling: Application to charge separation and charge recombination pathways in a model molecular donoracceptor system for organic solar cells. *J. Phys. Chem. C*, 112:3429–3433, 2008.

[163] T. Mančal, L. Valkunas, and G. R. Fleming. Theory of exciton-charge transfer state coupled systems. *Chem. Phys. Lett.*, 432:301–305, 2006.

[164] Marshall D. Newton. Quantum chemical probes of electron-transfer kinetics: the nature of donor-acceptor interactions. *Chem. Rev.*, 91:767–792, 1991.

[165] T. R. Prytkova, I. V. Kurnikov, and D. N. Beratan. Ab initio based calculations of electron-transfer rates in metalloproteins. *J. Phys. Chem B.*, 109:1618–1625, 2005.

[166] S. Larsson. Electron transfer in chemical and biological systems. orbital rules for nonadiabatic transfer. *J. Am. Chem. Soc.*, 103:4034–4040, 1981.

[167] E. K. U. Gross, J. F. Dobson, and M. Petersilka. null. *Top. Curr. Chem.*, 181:81, 1996.

[168] M. Head-Gordon, A. M. Graña, D. Maurice, and C. A. White. Analysis of electronic transtions as the difference of electron attachment and detachment densities. *J. Chem. Phys.*, 99:14261–14270, 1995.

[169] P.-O. Löwdin. Quantum theory of many-particle systems. i. physical interpretations by means of density matrices, natural spin-orbitals, and convergence problems in the method of configurational interaction. *Phys. Rev.*, 97(6):1474–1489, Mar 1955.

[170] D. J. Thouless. Stability conditions and nuclear rotations in the hartree-fock theory. *Nuc. Phys.*, 21:225–232, 1960.

[171] P. Peumans, V. Bulović, and S. R. Forrest. Efficient photon harvesting at high optical intensities in ultrathin organic double-heterostructure photovoltaic diodes. *Appl. Phys. Lett.*, 76:2650–2652, 2000.

[172] I. Kim, H. M. Haverinen, Z. Wang, S. Madakuni, Y. Kim, J. Li, and G. E. Jabbour. Efficient organic solar cells based on planar metallophthalocyanines. *Chem. Mater.*, 21:4256–4260, 2009.

[173] K. Triyana, T. Yasuda, F. Katsuhiko, and T. Tsutsui. Tandom-type organic solar cells by stacking different heterojunction materials. *Thin Solid Films*, 477:198–202, 2005.

[174] T. J. Schaafsma. Organic solar cells using porphyrin assemblies on semiconductor substrates. *Sol. Ener. Mat. Sol. Cells*, 38:349–351, 1995.

[175] P. Vilmercati, C. Castellarin Cudia, R. Larciprete, C. Cepek, G. Zampieri, L. Sangaletti, S. Pagliara, A. Verdini, A. Cossaro, L. Floreano, A. Morgante, L. Petaccia, S. Lizzit, C. Battocchio, G. Polzonetti, and A. Goldoni. Molecular orientations, electronic properties and charge transfer timescale in a zn-porphyrin/c70 donor-acceptor complex for solar cells. *Surface Science*, 600(18):4018–4023, 2006. Berlin, Germany: 4-9 September 2005, Proceedings of the 23th European Conference on Surface Science.

[176] F. Scandola, C. Chiorboli, A. Prodi, E. Iengo, and E. Alessio. Photophysical properties of metal-mediated assemblies of porphyrins. *Coord. Chem. Rev.*, 250:1471–1496, 2006.

[177] H. Fischer and H. Wenderoth. Optisch aktives hämotricarbonsäureimid aus chlorophyll. *Annalen*, 545:140–147, 1940.

[178] R. B. Woodward, W. A. Ayer, J. M Beaton, F. Bickelhaupt, R. Bonnett, P. Buchschacher, G. L. Closs, H. Dutler, J. Hannah, F. P. Hauck, Itô, S. A. Langemann, E. Le Goff, W. Leimgruber, W. Lwowski, J. Sauer, Z. Valenta, and H. Volz. The total synthesis of chlorophyll. *J. Am. Chem. Soc.*, 82:3800–3802, 1960.

[179] C. J. Cramer and D. G. Truhlar. Implicit solvation models: Equilibria, structure, spectra, and dynamics. *Chem. Rev.*, 99:2161–2200, 1999.

[180] J. Dai, J. M. Kanter, S. S. Kapur, W. D. Seider, and T. Sinno. On-lattice kinetic monte carlo simulations of point defect aggregation in entropically influenced crystalline systems. *Phys. Rev. B*, 72(13):134102, 2005.

Seth Difley

Tel: 857.928.2949 difley@mit.edu

Education

06/2004 – Present Massachusetts Institute of Technology, Cambridge, MA
Ph.D. candidate in Physical Chemistry
GPA: 5.0/5.0
Thesis topic: Computational modeling of organic solar cells and light-emitting device materials
Advisor: Prof. Troy Van Voorhis

01/2001 – 05/2004 University of Utah, Salt Lake City, UT
Bachelor of Science in Chemistry
Minor in Mathematics
GPA: 3.99/4.0, *Magna Cum Laude*
Research: Determination of buckminsterfullerene dianion stability by computer simulation
Mentor: Prof. Jack Simons

Research and Teaching Experience

06/2005 – Present Massachusetts Institute of Technology, Department of Chemistry, Cambridge, MA
RESEARCH ASSISTANT Studied energy conversion efficiency of organic solar cells using computer simulations, implemented models as computer programs, collaborated with experimentalists to validate simulation results and communicated technical outcomes by peer-reviewed articles, conference posters, and oral presentations.

06/2008 – 08/2008 Los Alamos National Laboratory, Theoretical Division, Los Alamos, NM
STUDENT RESEARCHER Used molecular mechanics simulations to study strategies for improving organic light-emitting device lifetimes. Presented two research lectures.
Mentor: Dr. Sergei Tretiak

Peer-reviewed Papers

Difley S., Wang L.-P., Yeganeh S., Yost S., and Van Voorhis T. "Electronic properties of disordered semiconductors via QM/MM simulations". *Accounts of Chemical Research*, submitted.

Difley S., Beljonne D. and Van Voorhis T. "On the singlet-triplet splitting of geminate electron-hole pairs in organic semiconductors". *Journal of the American Chemical Society*, *130*, 3420-3427, 2008.

Segal M., Singh M., Rivoire K., Difley S., Van Voorhis T. and Baldo M. A. "Extrafluorescent electroluminescence in organic light emitting devices". *Nature Materials*, 6, 374-378, 2007.

Difley S. and Simons J. "Role of angular electron pair correlation in stabilizing C_{60}^{2-}". *International Journal of Quantum Chemistry*, 108, 507-513, 2006.

Seth Difley

Presentations

INVITED LECTURE "Extending the lifetime of organic light emitting devices". CNLS Student Seminar Series, Los Alamos National Laboratory, Los Alamos, NM, USA. August 19, 2008.

INVITED POSTER "Charge-transfer state singlet-triplet splittings: Implications for organic light-emitting devices". Gordon Conference (Photochemistry), Bryant University, Smithfield, RI, USA. July 8-13, 2007.

POSTER "Charge-transfer/ exciton couplings in organic photovoltaics". 7th Canadian Computational Chemistry Conference, Dalhousie University, Halifax, Nova Scotia, Canada. July 20-24, 2009.

POSTER "Charge-transfer excited state energy splittings by constrained density functional theory". 6th Canadian Computational Chemistry Conference, University of British Columbia, Vancouver, British Columbia, Canada. July 26-30, 2006.

Volunteer Activities

09/2006 – Present Greater Boston Area Theoretical Chemistry Lecture Series
CO-ORGANIZER Invited theoretical chemistry lecturers, arranged schedules, managed budget, advertised lectures, and provided audio-visual assistance.

05/2007 – Present Chemistry Graduate Student Committee
COMMITTEE MEMBER Planned, advertised and hosted forums, social events and recruitment weekends for MIT Chemistry Department. Designed committee's website.

Honors and Awards

Phi Kappa Phi Honor Society
Golden Key Honor Society
Hypercube Scholar Award
American Institute of Chemists Award
Merit-based Tuition Waiver, University of Utah (2003-2004)
Eagle Scout, Boy Scouts of America